Lithos 340–341 (2019) 49–70

Contents lists available at ScienceDirect

Lithos

journal homepage: www.elsevier.com/locate/lithos

Petrogenesis of A-type granites associated with Sn–Nb–Zn mineralization in Ririwai complex, north-Central Nigeria: Constraints from whole-rock Sm—Nd and zircon Lu—Hf isotope systematics

Musa Bala Girei [a,b,c], Huan Li [b,*], Thomas J. Algeo [a,d,e], Bernard Bonin [f], Paul Olusegun Ogunleye [g], Saleh Ibrahim Bute [h], Hafizullah Abba Ahmed [d,i]

[a] Faculty of Earth Resources, State Key Laboratory of Geological Processes and Mineral Resources, China University of Geosciences, Wuhan 430074, China
[b] Key Laboratory of Metallogenic Prediction of Nonferrous Metals and Geological Environment Monitoring, Ministry of Education, School of Geosciences and Info-Physics, Central South University, Changsha 410083, China
[c] Department of Geology, Faculty of Earth and Environmental Sciences, Bayero University Kano, Kano State, Nigeria
[d] State Key Laboratory of Biogeology and Environment Geology, School of Earth Sciences, China University of Geosciences, Wuhan 430074, China
[e] Department of Geology, University of Cincinnati, Cincinnati, OH 42221-0013, USA
[f] UMR8148 'GEOPS', Université Paris-Sud, CNRS, Université Paris-Saclay, F-91405 Orsay Cedex, France
[g] Center for Energy Research and Training, Ahmadu Bello University Zaria, Nigeria
[h] Department of Geology, Gombe State University, P.M.B 127 Gombe, Gombe State, Nigeria
[i] Department of Geology, Modibbo Adama University of Technology, Yola, Adamawa State, Nigeria

ARTICLE INFO

Article history:
Received 28 November 2018
Accepted 3 May 2019
Available online 08 May 2019

Keywords:
Zircon U-Pb-Hf
ferroan
within-plate
Ring complex
Peralkaline
Aluminous

ABSTRACT

We report a combined study of whole-rock major- and trace-element geochemistry, Sm—Nd isotope composition, zircon U/Pb dating, and Lu—Hf systematics of peralkaline and aluminous A-type granites from the Ririwai Ring Complex in north-central Nigeria. The Ririwai peralkaline and aluminous A-type granites are strongly ferroan, alkalic to alkali-calcic, and enriched in Hf, Zr, Ga, Rb, Y and REEs. They were emplaced between 176 ± 2.3 Ma and 169.6 ± 0.75 Ma. The peralkaline granites yield relatively higher εNd(t) (−2.3 to −1.2) and zircon εHf(t) values (−5.8 to −1.7) than the aluminous granites (εNd(t) = −3.6 to −3.3; zircon εHf(t) = −7.8 to −2.4). In addition, inherited zircons in the aluminous granites yield Pan-African (~590 Ma) ages and low εHf (t) values (−14.0). Taken together, these data suggest that the granites formed from extensive fractional crystallization of a transitional basaltic melt derived from an enriched OIB mantle source. The depletions of MgO, CaO, Ti_2O, Sr and Ba in the granites indicate that Mg-rich olivine, calcic pyroxene, calcic amphibole, feldspars and Fe—Ti oxides were the major fractionated phases during magma evolution. In addition, several types of evidence, e.g., moderately negative εNd(t) and εHf(t) values, and the presence of inherited zircons, imply that the parental melt was modified by assimilation of Pan-African upper crust into which the granites were emplaced. A transtensional regime generated prior to late Jurassic breakup of Gondwana, which led to reactivation of shear zones and opening of associated transcurrent faults, paved the way for emplacement of the A-type suite. The Sn–Nb–Zn mineralization of the Ririwai A-type suite was probably linked to complex magmatic evolutionary processes involving extensive fractional crystallization coupled with crustal assimilation and late-stage hydrothermal fluid activity.

1. Introduction

Even though silica-oversaturated anorogenic granites and associated rocks commonly referred to as A-type granites (Loiselle and Wones, 1979) or ferroan granites (Frost et al., 2001) are volumetrically small, they occur widely in both continental and oceanic island settings as well as on other inner-Solar-system planets (Bonin, 2012). This igneous rock type has attracted considerable scientific and commercial interest globally owing to its association with economically significant Sn, W, Nb, U, and REE mineralization (Dall'Agnol et al., 2012; Dostal et al., 2014; Li et al., 2018a, 2018b). However, their petrogenesis remains in debate (Bonin, 2007; Martin, 2006). Largely due to their diverse mineralogical, chemical and isotopic compositions, distinctive petrogenetic models base on partial melting of diverse crustal sources (Creaser et al., 1991), fractional crystalllization of mantle-derived magmas (Bonin, 2007), and more complex scenarios involving mantle-crust interactions (Whalen et al., 1996) have been proposed for the origin of

* Corresponding author.
E-mail address: lihuan@csu.edu.cn (H. Li).

https://doi.org/10.1016/j.lithos.2019.05.003
0024-4937/

A-type granites. Based on their contrasting chemical compositions and tectonic settings, Eby (1992) subdivided A-type granites into A1 and A2 types. A1-type granites typically form from fractional crystallization of magmas derived from an enriched (OIB-like) mantle source in an intraplate setting, whereas A2-type granites are derivatives of partial melting of lower crust or crust-mantle interaction in post-collisional and/or post-orogenic settings (Eby, 1992).

This study focused on the source(s) of the peralkaline and aluminous A-type granites in the Ririwai Complex of Nigeria. The Ririwai Complex is one of >50 silica-oversaturated anorogenic syenite-granite ring complexes of Mesozoic age covering an area of 75,000 km^2 in north-central Nigeria that are collectively known as the "Nigerian Younger Granites". These ring complexes provide a useful natural laboratory for testing the origin of archetypal within-plate A-type granites (Ahmed et al., 2019; Bowden et al., 1987; Sakoma and Martin, 2011). Despite previous research, the magma source(s) and evolutionary processes of the Ririwai A-type granites still remain uncertain (Dickin et al., 1991; Ogunleye et al., 2006; Van Breemen et al., 1975). A complication in addressing these issues is that extensive hydrothermal alteration accompanying Sn–Nb–Zn mineralization of the granites has significantly perturbed their trace element and Sr—Pb isotope compositions. Consequently, whole-rock geochemical and Sr—Pb isotopic data (i.e., the major tools used by previous workers) failed to provide reliable constraints on the source(s) of the Ririwai A-type suite (Kinnaird and Bowden, 1991) [note: "suite" refers here to all Ririwai granites including both peralkaline and aluminous types]. The whole-rock Sm—Nd isotope system is fairly resistant to hydrothermal disturbances (Dickin et al., 1991) and can constrain magma source(s) for A-type granites, especially when combined with zircon Lu—Hf isotopes (Kemp et al., 2005). In this paper, we present, for the first time, zircon U—Pb age and Lu—Hf isotope data as well as new whole-rock Sm—Nd data for the Ririwai peralkaline and aluminous granites. In addition, previously published Sm—Nd isotope data on Nigerian basement rocks (Dada et al., 1995) and A-type granites (Dickin et al., 1991) were re-evaluated along with the new data in order to better constrain the source(s) of the Ririwai A-type granites and their associated Sn–Nb–Zn mineralization.

2. Regional geological setting

The "Nigerian Younger Granites" comprise >50 silica-oversaturated anorogenic syenite-granite ring complexes of Mesozoic age (Fig. 1a, b). They cover a total area of 75,000 km^2 in north-central Nigeria and occupy a 400-km-long, 160-km-wide, north-trending belt between latitudes 8°N and 12°N and longitudes 8°E and 10°E (Bowden et al., 1987). The distribution of these alkaline ring complexes is controlled mainly by a network of N-S-trending megashear zones and associated deep-seated transcurrent faults created during the waning stages of the Pan-African Orogeny (600 ± 150 Ma), during which Gondwana amalgamated (Black et al., 1985; Black and Liégeois, 1993).

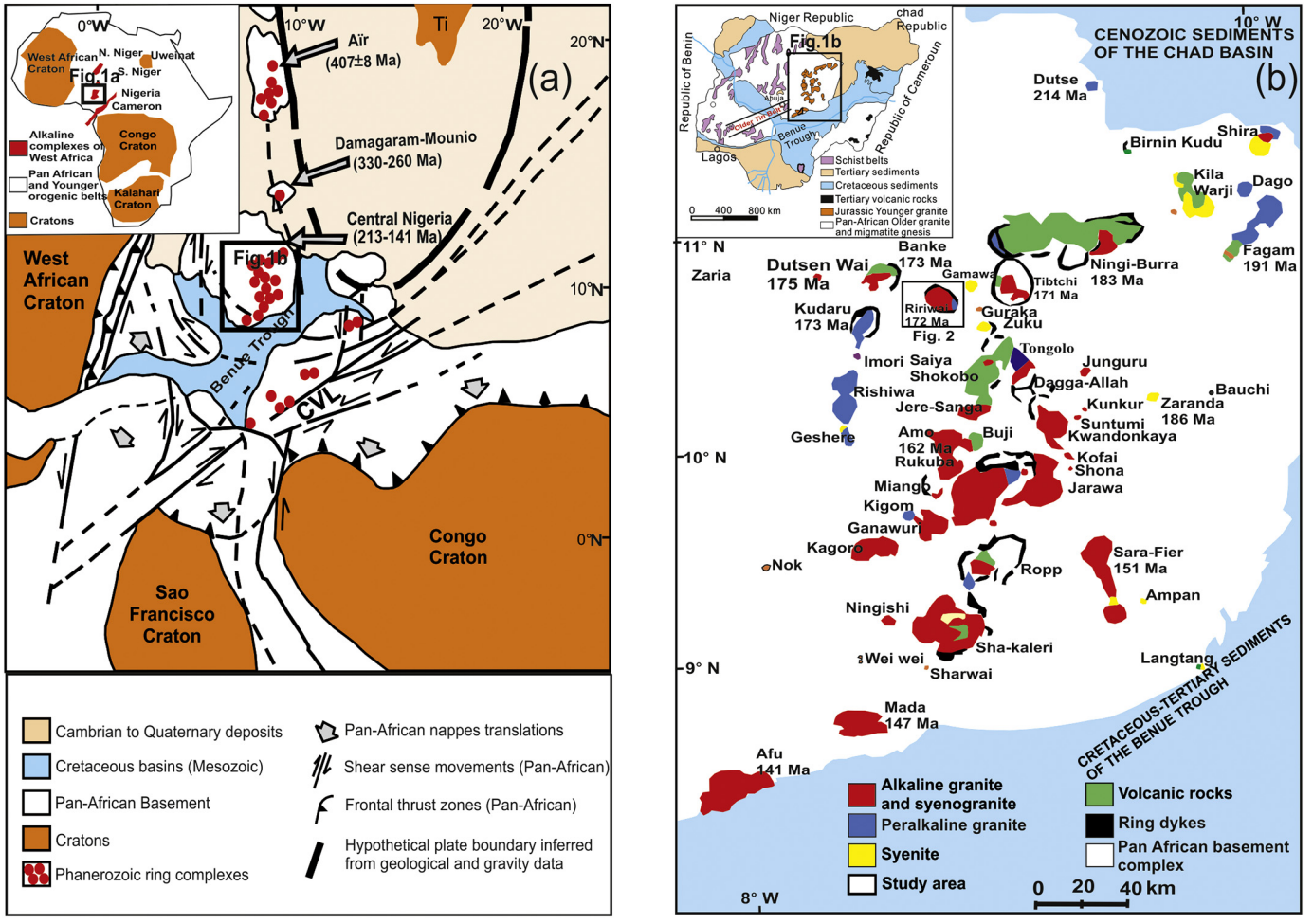

Fig. 1. (a) Sketch map showing the distribution of Phanerozoic anorogenic ring complexes in Aïr (northern Niger), Damagaram-Mounio (southern Niger), north-central Nigeria, and Cameroon in relation to Pan-African continental structures of Western Gondwana (redrawn from Ngako et al., 2006). Note the N-S decreasing age trend from northern Niger to Nigeria. "CVL" is an abbreviation for Cameroon Volcanic Line. (b) Simplified geological map showing the distribution of anorogenic ring complexes in north-central Nigeria (modified from Kinnaird et al., 1985). Block box shows the location of Fig. 2.

In the Adrar des Iforas of Mali, silica-oversaturated alkaline magmatism commenced just ~10 Myr after the Pan-African Orogeny and lasted for ~20 Myr (Black et al., 1985). In contrast, alkaline ring complexes in the Niger-Nigeria province were emplaced long after the Pan-African Orogeny (Kinnaird and Bowden, 1991). Emplacement ages decrease from north to south, ranging from Ordovician-Devonian (480–400 Ma) in Aïr (northern Niger) to Carboniferous (330–260 Ma) in Damagaram-Mounio (southern Niger) to Triassic-Early Cretaceous (213–141 Ma) in north-central Nigeria (Fig. 1a, b; Kinnaird and Bowden, 1991). To the southeast, the Cenozoic (73 Ma to Recent) Cameroon Volcanic Line is separated from the Nigerian ring complexes by the Cretaceous Benue Trough (Ngako et al., 2006; Fig. 1a). Elsewhere in Africa (e.g., Egypt, Sudan, Ethiopia, and Damaraland in Namibia), anorogenic ring complexes do not show any spatial age progression but, instead, episodically recurrent activity at different times in different places (Martin et al., 2012; Trumbull et al., 2004).

The Nigerian ring complexes range in diameter from 2 to 25 km. They crosscut the Precambrian basement of the eastern Nigerian terrain, which consists mainly of migmatite, gneiss, and metapelite of Paleoproterozoic (Eburnian) age with relics of Archean rocks, as well as Pan-African *syn*-collisional to post-collisional granites, monzodiorites, and charnockites of largely crustal origin (Dada et al., 1995; Dickin et al., 1991; Ferré et al., 1998; Ferré and Caby, 2007). The post-collisional granites in Nigeria are spatially associated with Sn–Nb–Ta mineralized pegmatites that are largely concentrated along a NE-SW-trending zone known as the "Older Tin Belt" (Küster, 1990; Fig. 1b).

The anorogenic activity started to the north in the Dutse complex during the Triassic (~213 Ma, Norian) and lasted until the Early Cretaceous (~141 Ma, Berriasian) in the Afu complex near the Benue Trough. The Niger-Nigerian alkaline province has been regarded as an epizonal equivalent of anorthosite-mangerite-charnockite-granite (AMCG) suites (Magaji et al., 2011; Martin et al., 2012), but, unlike in Aïr, Niger, anorthosite occurs only as xenoliths within dolerite dykes near the Jos Plateau, Nigeria (Bowden et al., 1987). The igneous activity started with a succession of eruptive events, marked by comendites and ignimbritic rhyolites (Bowden and Kinnaird, 1984). Rare hawaiites, mugearites, and trachytes occur in some centres (Kinnaird and Bowden, 1991). Later caldera collapse paved the way for emplacement of epizonal syenite-granite associations forming circular to elliptical ring complexes (Bowden et al., 1987).

Except in syenite-bearing anorogenic centres, fayalite hedenbergite granite porphyry, which occupies outer ring-faults, represents the oldest plutonic unit (Bowden and Kinnaird, 1984). It is preceded only by volcanic feeder intrusions, consisting of quartz porphyries welded in cone sheets or ring faults (Bowden et al., 1987). Emplacement of fayalite hedenbergite granite porphyry is followed by multiple intrusions of peralkaline granites, except in the southern centres where peralkaline granites are absent. Aluminous biotite granites, volumetrically dominant in most plutonic suites, are invariably the youngest units (Van Breemen et al., 1975). They have experienced a cooling history punctuated by multi-stage hydrothermal activity with deposition of cassiterite, columbite, wolframite ores and minor Pb–Zn–Cu sulphide mineralization (Bowden et al., 1987). Primary Sn–Nb–W–Zn lodes occur in Ririwai, Tibchi, and Afu complexes (Kinnaird et al., 2016).

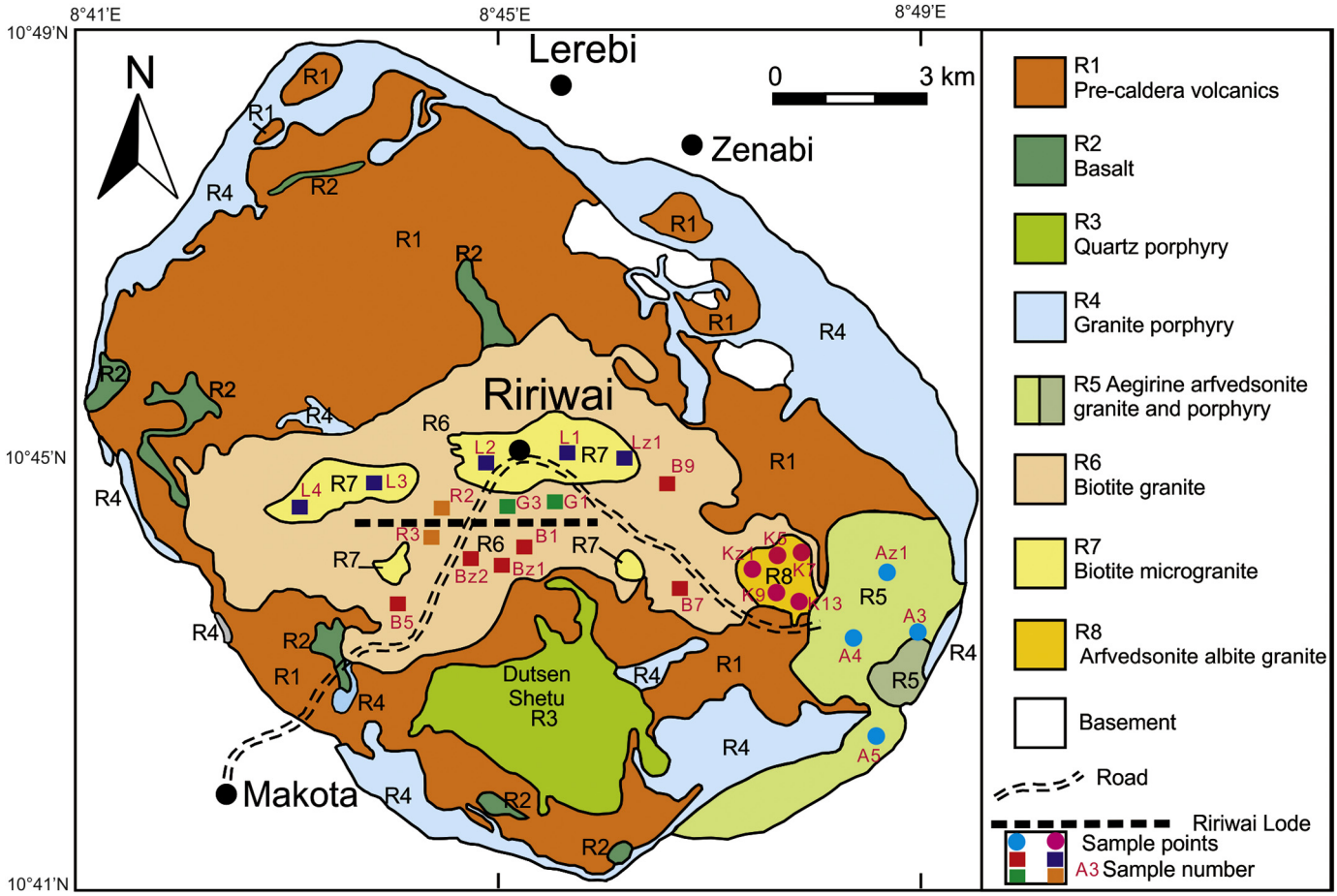

Fig. 2. Geological map of the Ririwai anorogenic ring complex (modified from Kinnaird et al., 1985).

Subsequently, rare-metal ores were unroofed, eroded and concentrated in alluvial placer deposits.

3. Local geology and petrographic characteristics

3.1. Geology of the Ririwai Complex

The Ririwai Complex occupies a total area of 180 km^2 (Fig. 1b). It is elliptical in shape, with semi-major and semi-minor axes measuring 15 km and 11 km, respectively. It is composed of an outer ring-dyke of granite porphyry surrounding down-faulted basement and volcanic rocks and a core of arfvedsonite aegirine, arfvedsonite albite and biotite granites (Fig. 2). Detailed descriptions of the petrology and structural evolution of this complex have been provided by Jacobson et al. (1958), Jacobson and McLeod (1977), Martin and Bowden (1981), and Kinnaird et al. (1985).

The magmatic activity started with the extrusion of a large volume of rhyolitic ignimbrite, followed by ring-fracturing, block subsidence, and formation of a large cauldron in which volcanics accumulated. The volcanic assemblages consist largely of ignimbritic rhyolite and comendite (R1), with minor olivine basalt (R2). During the waning stage of the volcanic cycle, a large plug of quartz-porphyry (R3) was emplaced in the centre of Dutsen Shetu vent complex (Jacobson and McLeod, 1977). The plutonic cycle started with the intrusion of granite porphyry (R4) that occupies the outer ring-dyke. It was followed successively by intrusions of aegirine arfvedsonite granite (R5), arfvedsonite albite granite (R8), biotite granite (R6), and biotite microgranite (R7) (Fig. 2).

The aegirine arfvedsonite granite (R5) has an outcrop area of 10.4 km^2 and is confined to the southeastern corner of the ring complex (Fig. 2). It is intrusive into the rhyolites. South of Kaffo, the granite contains numerous large blocks of rhyolite. North of Kaffo, the contact of the arfvedsonite aegirine granite dips steeply to the west, and numerous dykelets of biotite granite crosscut the adjacent rhyolites. Several small intrusions of arfvedsonite microgranite occur in the eastern part of the ring complex. The largest of these intrusive bodies is 0.8 km long and oriented parallel with the southeastern margin of the complex.

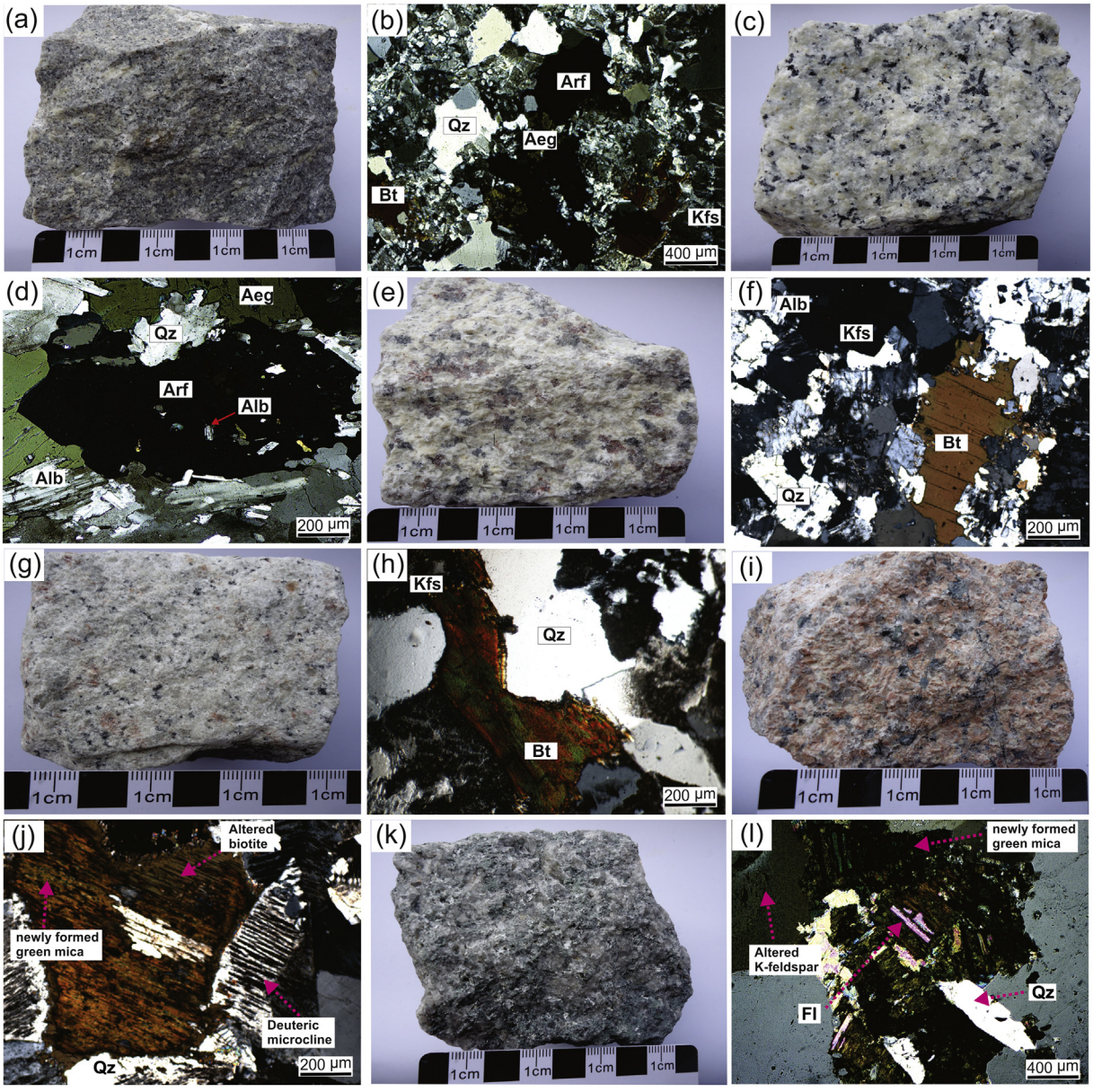

Fig. 3. Photographs of hand specimens and photomicrographs of (a-b) aegirine arfvedsonite granite; (c-d) aegirine albite granite; (e-f) biotite granite; (g-h) biotite microgranite; (i-j) reddened granite, (k-l) mica quartz greisen from Ririwai complex. Qz = quartz, Bt = biotite, Kfs = K-feldspar, Aeg = aegirine, Arf = arfvedsonite, Alb = albite, Fl = fluorite.

Table 1
Major and trace element compositions of A-type granites of Ririwai complex.

Rock type	JG-2	Aegirine arfvedsonite granite				Arfvedsonite albite granite					Biotite granite						Biotite microgranite					Reddened granite		Quartz-mica Greisen	
Samples	standard	AZ1	A3	A4	A5	KZ1	K5	K7	K9	K13	BZ1	BZ2	B1	B5	B7	B9	LZ1	L1	L2	L3	L4	R2	R3	G1	G3
SiO_2	76.83	76.54	76.74	76.32	76.57	72.31	72.84	70.71	72.96	70.17	76.48	76.33	76.8	76.63	76.63	77.46	77.49	77.24	75.63	77.26	76.68	76.12	76.92	93.09	91.33
TiO_2	0.044	0.15	0.15	0.15	0.15	0.06	0.1	0.13	0.08	0.09	0.06	0.05	0.05	0.05	0.05	0.06	0.06	0.05	0.06	0.06	0.06	0.06	0.07	0.06	0.03
Al_2O_3	12.47	11.02	11.04	11.01	10.96	12.32	11.41	13.26	12.18	13.98	12.1	11.92	11.93	12.14	11.99	12.26	12.16	12.32	12.78	12.2	12.6	12.2	12.38	1.78	2.53
Fe_2O_3T	1.18	3.07	2.99	2.95	2.88	3.22	3.03	2.47	2.66	2.54	2.21	1.99	1.98	1.86	1.67	1.62	1.81	1.82	1.96	1.82	1.74	2.34	1.99	3.94	4.49
MnO	0.02	0.04	0.04	0.04	0.04	0.05	0.07	0.04	0.05	0.05	0.02	0.02	0.02	0.02	0.02	0.02	0.02	0.02	0.02	0.02	0.02	0.03	0.03	0.04	0.04
MgO	0.04	0.04	0.04	0.02	0.03	0.04	0.04	0.03	0.04	0.04	0.02	0.01	0.03	0.03	0.05	0.04	0.02	0.03	0.02	0.03	0.03	0.04	0.03	0.03	0.02
CaO	0.7	0.38	0.31	0.39	0.38	0.04	0.1	0.02	0.03	0.02	0.3	0.34	0.35	0.06	0.06	0.05	0.05	0.04	0.05	0.05	0.13	0.18	0.29	0.17	0.02
Na_2O	3.54	3.94	3.89	3.95	3.9	6.36	5.6	6.98	6.33	7.29	4.19	4.1	4.07	4.1	4.09	4.1	3.94	3.79	2.77	3.76	3.18	3.22	4.02	0.05	0.04
K_2O	4.71	4.49	4.52	4.49	4.45	3.73	4.42	4.39	3.76	3.78	4.38	4.26	4.33	4.29	4.26	4.41	4.28	4.42	4.67	4.28	4.58	5.09	4.44	0.4	0.57
P_2O_5	0.002	0.03	0.02	0.01	0.02	0.04	0.03	0.01	0.03	0.04	0.01	0.01	0.03	0.01	0.01	0.02	0.02	0.01	0.01	0.03	0.02	0.02	0.01	0.01	0.01
L.O·I	4.56	0.33	0.37	0.33	0.36	0.73	0.86	0.71	0.67	0.86	0.26	0.34	0.39	0.33	0.4	0.39	0.56	0.55	1.22	0.54	1.05	0.59	0.53	0.58	0.66
Total		99.70	99.8	99.36	99.44	98.59	98.18	98.5	98.52	98.58	99.81	99.17	99.76	99.33	99.06	100.26	100.22	100.11	98.99	99.85	99.91	99.65	100.51	99.76	99.29
Na2O + K2O		8.43	8.41	8.44	8.35	10.09	10.02	11.37	10.09	11.07	8.57	8.36	8.4	8.39	8.35	8.51	8.22	8.21	7.44	8.04	7.76	8.31	8.46	0.45	0.61
K2O/Na2O		1.14	1.16	1.14	1.14	0.59	0.79	0.63	0.59	0.52	1.05	1.04	1.06	1.05	1.04	1.08	1.09	1.17	1.69	1.14	1.44	1.58	1.1	8	14.25
A/CNK		0.92	0.9	0.9	0.9	0.9	0.8	0.8	0.8	0.9	1.0	1.0	1.0	1.1	1.1	1.1	1.1	1.1	1.3	1.1	1.2	1.1	1.0	2.2	3.5
A.I		1.03	1.02	1.03	1.02	1.18	1.23	1.22	1.19	1.15	0.96	0.95	0.95	0.94	0.95	0.94	0.91	0.89	0.75	0.89	0.81	0.89	0.92	0.29	0.27
TZr/°C		997	1007	981	978	1051	1207	1075	1119	1062	854	850	849	852	850	842	848	830	838	838	867	847	860	930	905
Q		34.58	34.90	34.50	35.02	24.89	28.44	20.13	26.41	17.45	33.46	34.33	34.68	35.14	35.4	35.67	37.05	37.13	40.41	37.84	39.36	36.13	34.76	88.58	86.22
C		0.00	0.00	0.00	0.00	0.02	0.00	0.00	0.02	0.00	0.00	0.00	0	0.67	0.57	0.67	0.98	1.25	3.1	1.31	2.2	1.09	0.46	0.98	1.83
Ac		1.2	1.14	1.15	1.12	1.26	1.18	0.96	1.04	0.99	0.00	0.00	0	0	0	0	0	0	0	0	0	0	0	0	0
Ga	18.6	46.4	47.5	45.2	44.7	71.8	62.9	73.1	70.8	86.4	51.8	51.9	51.6	51.5	52.2	51.8	57.9	57.6	59.3	54.9	58.2	53.1	53.2	25.2	35.4
Nb	14.7	307.0	291.0	307.0	304.0	878.0	526.0	1640.0	1415.0	1915.0	199.0	234.0	190.5	230.0	182.5	199.0	134.5	133.0	134.0	128.0	134.5	180.0	187.5	317.0	179.5
Ta	2.8	37.6	30.3	42.5	41.5	94.4	41.3	174.5	152.0	211.0	22.7	24.7	22.3	24.7	20.0	21.0	12.8	15.9	13.2	12.2	15.6	16.6	16.1	22.7	24.8
W	23.0	3.0	3.0	3.0	3.0	6.0	4.0	11.0	9.0	11.0	3.0	2.0	2.0	3.0	2.0	2.0	1.0	2.0	1.0	1.0	2.0	7.0	3.0	9.0	4.0
Sn	3.0	38.0	56.0	43.0	34.0	205.0	167.0	181.0	168.0	144.0	42.0	42.0	43.0	62.0	46.0	30.0	17.0	19.0	17.0	15.0	22.0	227.0	63.0	63.0	39.0
Rb	301.0	449.0	450.0	448.0	458.0	1190.0	1535.0	1415.0	1225.0	1410.0	623.0	652.0	661.0	553.0	562.0	577.0	562.0	565.0	606.0	537.0	618.0	808.0	606.0	245.0	374.0
Sr	17.9	8.2	7.3	7.8	7.5	1.1	3.2	1.1	1.5	1.2	0.9	6.2	6.5	3.0	2.9	2.8	0.9	2.3	2.4	1.3	1.8	2.2	1.1	1.1	0.5
Ba	81.0	33.3	35.0	25.3	21.7	3.5	9.8	5.1	3.8	2.7	2.1	5.8	6.1	232.0	176.5	373.0	1.4	4.4	3.1	1.7	2.0	6.2	2.1	1.0	1.8
Cs	6.8	6.0	7.4	7.7	6.5	2.1	14.2	5.0	2.8	7.5	5.0	3.9	4.0	4.7	4.6	4.1	4.6	4.8	5.0	4.3	5.5	3.9	2.8	3.5	4.6
Pb	31.5	99.2	92.8	101.9	96.9	185.7	92.9	278.6	278.6	185.7	92.9	97.9	93.9	92.9	92.9	92.9	89.9	96.9	90.4	94.5	79.8	1021.4	98.3	92.9	91.6
Cr	6.4	10.1	9.8	10.0	10.0	10.1	10.0	10.1	10.1	8.8	10.0	10.0	10.0	9.9	10.0	8.9	7.6	9.8	10.0	7.3	8.1	4.7	6.2	9.1	9.0
V	3.8	4.6	12.0	4.2	5.0	4.9	4.2	6.0	7.0	5.0	7.0	4.0	4.7	5.0	4.9	4.5	9.0	5.0	4.9	7.0	4.0	4.1	4.0	5.1	5.0
Hf	4.7	39.3	44.3	35.0	31.9	95.6	272.0	129.5	151.0	103.0	19.4	18.8	18.6	18.4	18.0	16.2	14.0	13.6	11.7	12.9	16.8	15.0	18.5	17.6	16.1
Zr	97.6	1290.0	1370.0	1140.0	1100.0	2370.0	6940.0	3150.0	3840.0	2650.0	328.0	314.0	311.0	298.0	295.0	271.0	276.0	224.0	206.0	241.0	300.0	272.0	332.0	316.0	214.0
Y	86.5	258.0	270.0	251.0	248.0	1100.0	728.0	145.5	795.0	210.0	152.5	206.0	211.0	35.6	35.9	28.2	25.9	31.8	25.5	22.4	34.4	111.0	167.0	115.5	22.0
Th	31.6	60.5	90.0	62.4	45.3	138.5	263.0	156.0	200.0	148.0	54.0	56.2	53.2	41.0	41.4	22.0	26.4	31.4	23.2	24.9	32.2	39.6	52.6	59.0	32.7
U	11.3	23.6	17.2	22.0	25.0	78.1	33.1	155.5	124.5	190.0	14.3	13.2	12.6	9.8	9.2	8.3	9.7	9.9	7.3	8.3	11.5	11.1	15.0	16.5	5.6
La	19.9	108.5	104.0	98.3	96.6	69.4	39.1	110.5	93.9	90.4	58.0	65.0	66.2	60.0	52.9	32.6	26.8	40.4	12.1	20.4	26.1	60.6	58.3	56.4	34.6
Ce	48.3	228.0	216.0	208.0	206.0	188.0	106.0	310.0	259.0	272.0	107.5	117.5	116.5	93.4	83.3	51.0	46.3	70.4	19.8	35.0	45.3	113.5	111.5	110.5	63.8
Pr	6.2	28.4	26.3	25.9	25.0	23.7	14.2	33.5	29.9	29.8	11.0	13.3	13.0	8.1	7.3	4.5	4.4	6.9	1.9	3.2	4.3	12.0	11.9	11.6	6.4
Nd	26.4	108.0	99.3	97.8	94.1	85.3	57.2	96.5	97.4	87.1	34.9	43.4	43.6	21.4	19.6	12.2	12.0	19.8	5.2	8.7	11.8	37.7	37.0	36.4	19.5
Sm	7.8	29.7	26.7	25.9	25.8	38.0	30.9	26.5	34.7	31.3	9.2	11.8	11.7	3.2	3.2	2.0	2.6	4.1	1.0	1.8	2.7	9.5	10.2	9.5	4.7
Eu	0.1	1.3	1.2	1.2	1.1	1.7	1.4	0.9	1.3	1.1	0.1	0.3	0.3	0.1	0.1	0.1	0.0	0.1	0.0	<0.03	0.0	0.2	0.1	0.1	0.1
Gd	8.0	34.3	30.3	31.3	30.2	58.3	61.8	21.1	44.1	30.1	11.3	15.4	15.3	3.0	2.8	2.2	2.5	3.9	1.5	1.8	2.8	10.5	12.3	10.2	4.3
Tb	1.6	6.7	6.3	6.2	5.9	19.1	18.1	5.2	14.1	8.5	2.6	3.5	3.6	0.6	0.6	0.5	0.6	0.8	0.4	0.4	0.6	2.3	2.7	2.3	0.8
Dy	10.5	41.1	39.8	38.3	37.1	161.0	133.5	32.9	115.0	53.3	18.0	25.4	25.2	4.0	4.1	3.3	3.4	4.6	2.7	2.7	4.0	14.4	19.9	14.4	4.3
Ho	1.7	8.8	8.9	8.5	8.0	42.2	30.4	6.8	28.9	10.4	4.1	6.2	6.1	1.0	1.0	0.8	0.7	1.0	0.7	0.6	0.9	3.1	4.6	3.1	0.8
Er	6.0	26.4	27.3	25.3	24.3	155.0	88.7	22.0	105.0	29.5	14.1	21.4	21.1	3.5	3.4	2.9	2.7	3.1	2.5	2.3	3.4	10.4	14.7	10.3	2.3
Tm	1.2	4.1	4.5	4.0	3.9	28.1	12.5	4.4	19.2	4.6	2.4	3.6	3.6	0.6	0.7	0.5	0.5	0.6	0.5	0.5	0.7	1.8	2.6	1.9	0.4
Yb	6.9	24.4	28.1	24.0	22.9	162.5	69.1	36.1	117.0	26.1	16.1	23.3	23.3	4.2	4.2	3.8	4.0	4.0	3.6	3.5	4.9	11.3	16.7	12.6	2.6
Lu	1.2	3.6	4.1	3.5	3.5	20.7	9.5	7.1	15.0	3.8	2.5	3.6	3.5	0.8	0.7	0.7	0.7	0.7	0.6	0.6	0.8	1.7	2.6	1.9	0.4
£REE		653.3	622.9	598.2	584.3	1052.9	672.3	713.5	974.5	677.9	291.7	353.6	353.1	203.9	183.9	117.0	107.2	160.3	52.6	81.6	108.3	288.8	304.9	281.0	144.9
(La/Sm)cn		2.3	2.4	2.3	2.3	1.1	0.8	2.6	1.7	1.8	3.9	3.4	3.5	11.7	10.2	10.0	6.3	6.1	7.2	6.8	5.9	3.9	3.5	3.7	4.5
(Gd/Yb)cn		1.1	0.9	1.0	1.1	0.3	0.7	0.5	0.3	0.9	0.6	0.5	0.5	0.6	0.5	0.5	0.5	0.8	0.3	0.4	0.5	0.7	0.6	0.6	1.3
(La/Yb)cn		3.0	2.5	2.7	2.8	0.3	0.4	2.0	0.5	2.3	2.4	1.9	1.9	9.5	8.4	5.8	4.5	6.8	2.2	3.9	3.6	3.6	2.3	3.0	8.9
(Eu/Eu)*		0.1	0.1	0.1	0.1	0.1	0.1	0.1	0.1	0.1	0.04	0.1	0.1	0.1	0.1	0.1	0.1	0.1	0.1	0.1	0.1	0.1	0.0	0.0	0.1

Note: Fe_2O_3T = FeOt/0.8998, C=CIPW normative corundum, Q = normative quartz, Ac = normative acmite, A.I = agpaitic index.
Note: All oxide are in weight percent (wt%), while trace element are in part per million (ppm).

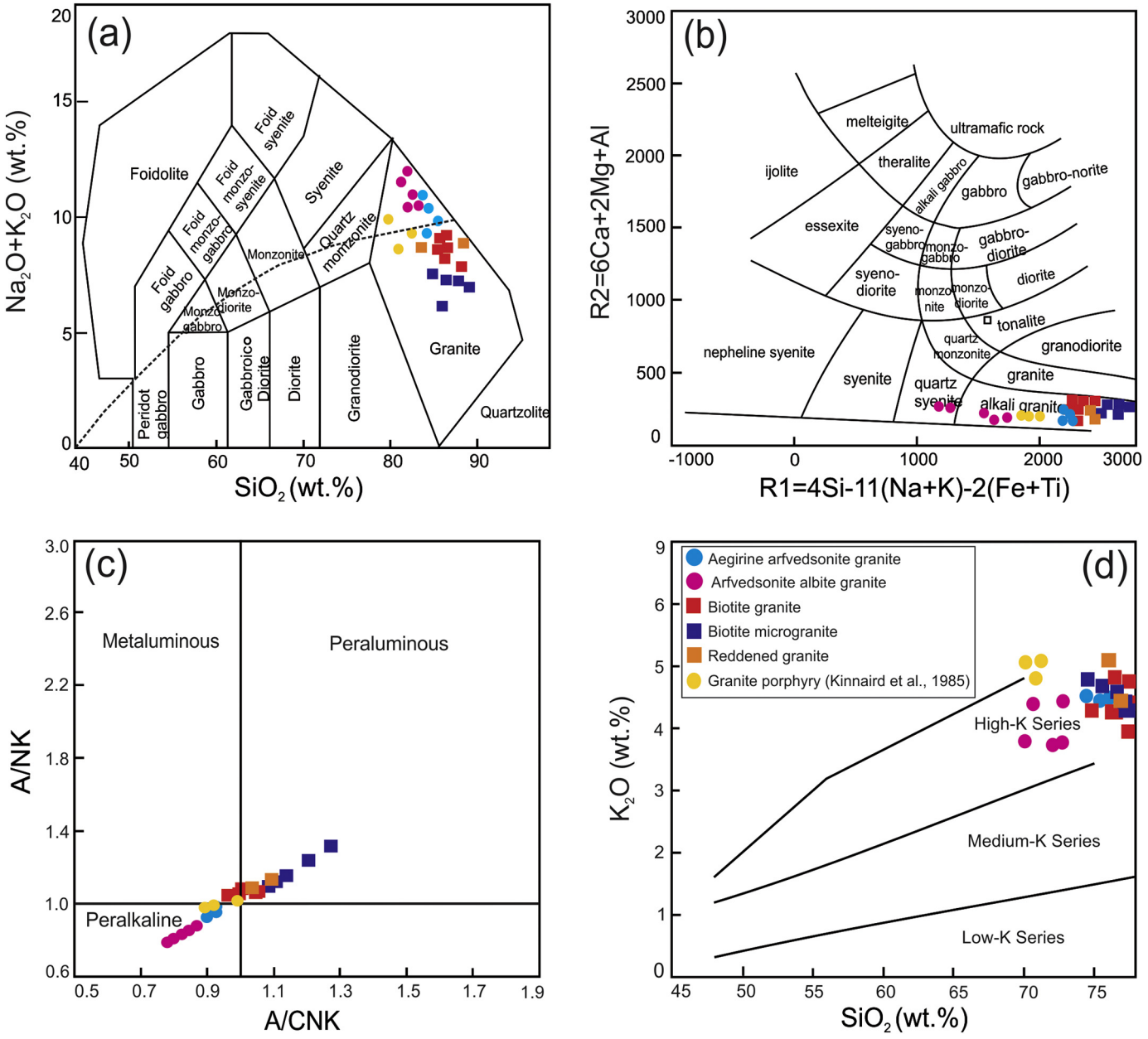

Fig. 4. Granite classification diagrams. (a) SiO_2 vs. $Na_2O + K_2O$ (after Le Maitre, 1989), (b) R1 vs. R2 (after De la Roche et al., 1980), (c) A/CNK vs. A/NK (after Shand, 1943), (d) SiO_2 vs. K_2O (after Peccerillo and Taylor, 1976).

The arfvedsonite albite granite (R8) occupies an outcrop area of 1.3 km^2 and lies between biotite granite to the west and aegirine arfvedsonite granite to the east (Fig. 2). The contact of the arfvedsonite albite granite is marked by the development of a pegmatitic phase. Pegmatites do not form a continuous band but rather a series of elongated pegmatitic knots set in a fine-grained groundmass.

The biotite granites (R6) occupy an area of ~31 km^2 in the centre of the complex (Fig. 2). They have long been the object of scientific and economic inquiry, because they host lodes with estimated reserves of 2,830,351 tons of cassiterite and sphalerite at average grades of 0.61% Sn and 2.05% Zn, and displays significant concentrations of other rare metals such as Nb and W (Kinnaird et al., 1985, 2016). The main intrusion is medium-grained and equigranular and shows only minor variations in texture. Two other intrusive bodies, Liruei granite and Korako microgranite (R7), are distinguished within the main mass. The Liruei Granite is slightly finer in grain size than the main granite and host several small intrusions of microgranite with well-developed contacts. The main fracture system strikes east-west, with subvertical dips, and is parallel with lode mineralization and related quartz veins.

3.2. Petrographic characteristics of Ririwai Complex granites

The aegirine arfvedsonite granite is medium- to coarse-grained, greyish to yellowish in colour, and contains large ragged plates of arfvedsonite intergrown with aegirine (Fig. 3a). In thin section, the essential minerals are quartz (30–35%), orthoclase mesoperthite (55–60%), albite (3.5 to 4%), arfvedsonite (2 to 2.5%), aegirine (2.5 to 3%), and biotite (1 to 2%), with zircon, astrophyllite and fluorite as accessory minerals. In terms of crystallization sequence, feldspar and quartz precipitated first, followed by aegirine and arfvedsonite. Quartz grains are angular and relatively free from inclusions (Fig. 3b). The major feldspar is a typical exsolution mesoperthite of orthoclase and albite. It forms large anhedral crystals that are twinned and may include rounded blebs of quartz. Rims of poorly twinned secondary albite are occasionally

present. Aegirine forms spongy sieve crystals that enclose feldspar crystals. Arfvedsonite is similar in habit, and the two minerals are frequently intergrown. Euhedral grains of aegirine are often found in small interstitial patches of quartz. Astrophyllite is a ubiquitous accessory mineral in variable amounts. It forms small elongated flakes often arranged in fan-like shapes. Zircon is another common accessory, and fluorite is also present.

The arfvedsonite albite granite is a medium-grained, light-coloured rock, flecked with needle-like crystals of arfvedsonite that are distributed randomly through the matrix of quartz, feldspar, and subordinate aegirine (Fig. 3c). It differs from the arfvedsonite aegirine granite in (1) precipitation of albite throughout its crystallization history and (2) rapid crystallization of all minerals during the late cooling stage. Its texture varies by shape and distribution of arfvedsonite crystals. The essential minerals are quartz (30–32%), orthoclase mesoperthite (39–41%), albite (16–17%), arfvedsonite (7–8.5%), and aegirine (1 to 2%). Alkali feldspar and quartz were the first minerals to crystallize, followed by primary albite. Aegirine was deposited before arfvedsonite. Quartz grains show frequently a zone of minute inclusions of fluorite. Feldspar consists of a cloudy, mottled perthitic intergrowth of albite and orthoclase of both exsolution and replacement types. Microcline is occasionally present. Intergrowths of quartz and feldspar are rare, although one sample (K9) exhibits a micrographic intergrowth. Primary albite occurs as well-twinned crystals forming a fine interlacing network between quartz, orthoclase mesoperthite, and arfvedsonite, and is occasionally enclosed within large arfvedsonite crystals (Fig. 3d). Secondary albite forms non-twinned crystals replacing early-formed orthoclase or quartz. Aegirine is subordinate to and surrounded by arfvedsonite, but, in limited areas, aegirine is dominant and surrounds arfvedsonite. The main accessory minerals include pyrochlore, cryolite, amblygonite, zircon, and monazite. Cryolite and pyrochlore were commonly the last phases to crystallize. Cryolite is interstitial, as a growth

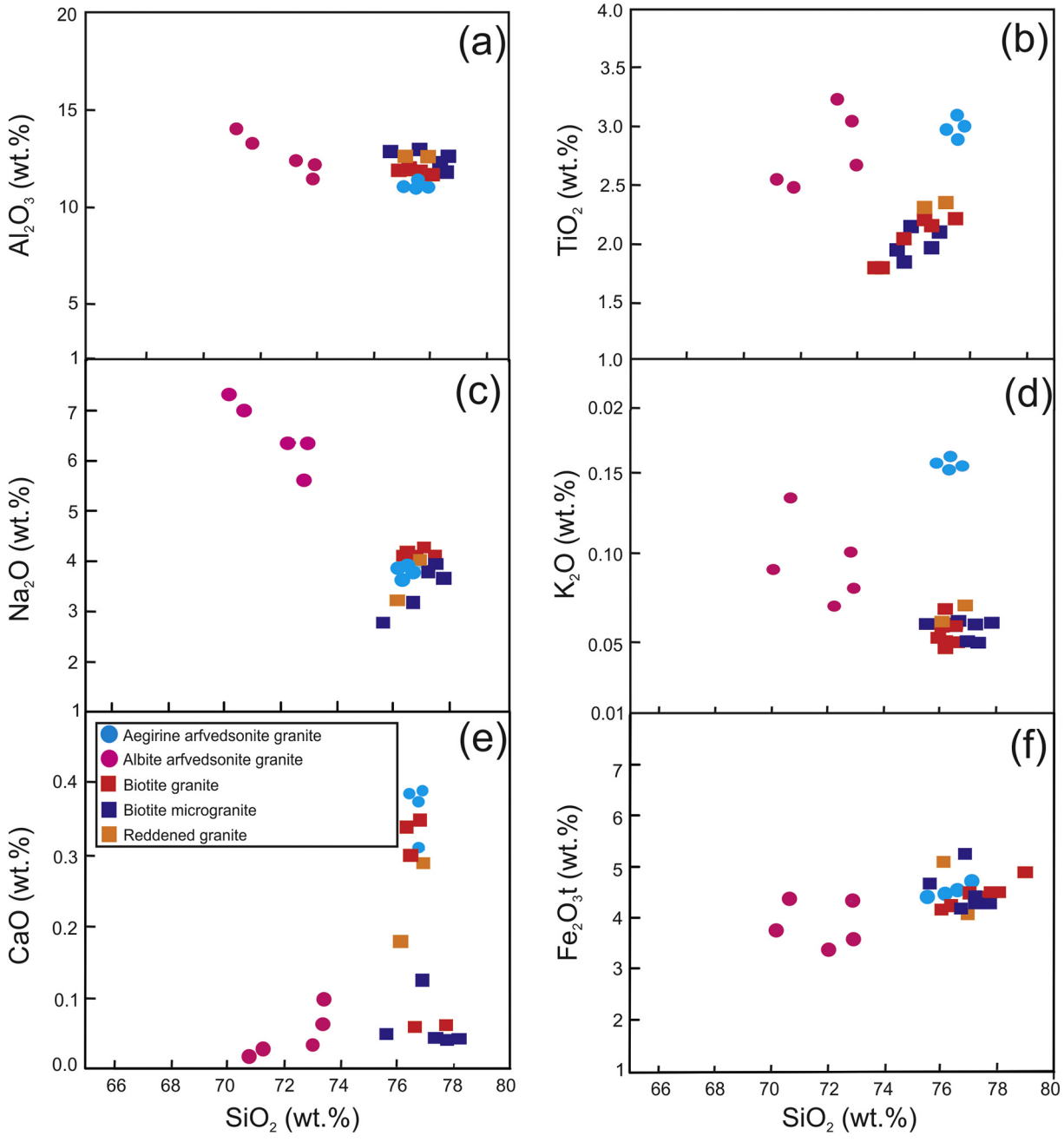

Fig. 5. Harker plots of SiO_2 vs. (a) Al_2O_3, (b) TFe_2O_3, (c) MgO, (d) TiO_2, (e) Na_2O, (f) K_2O, (g) CaO, and (h) P_2O_5.

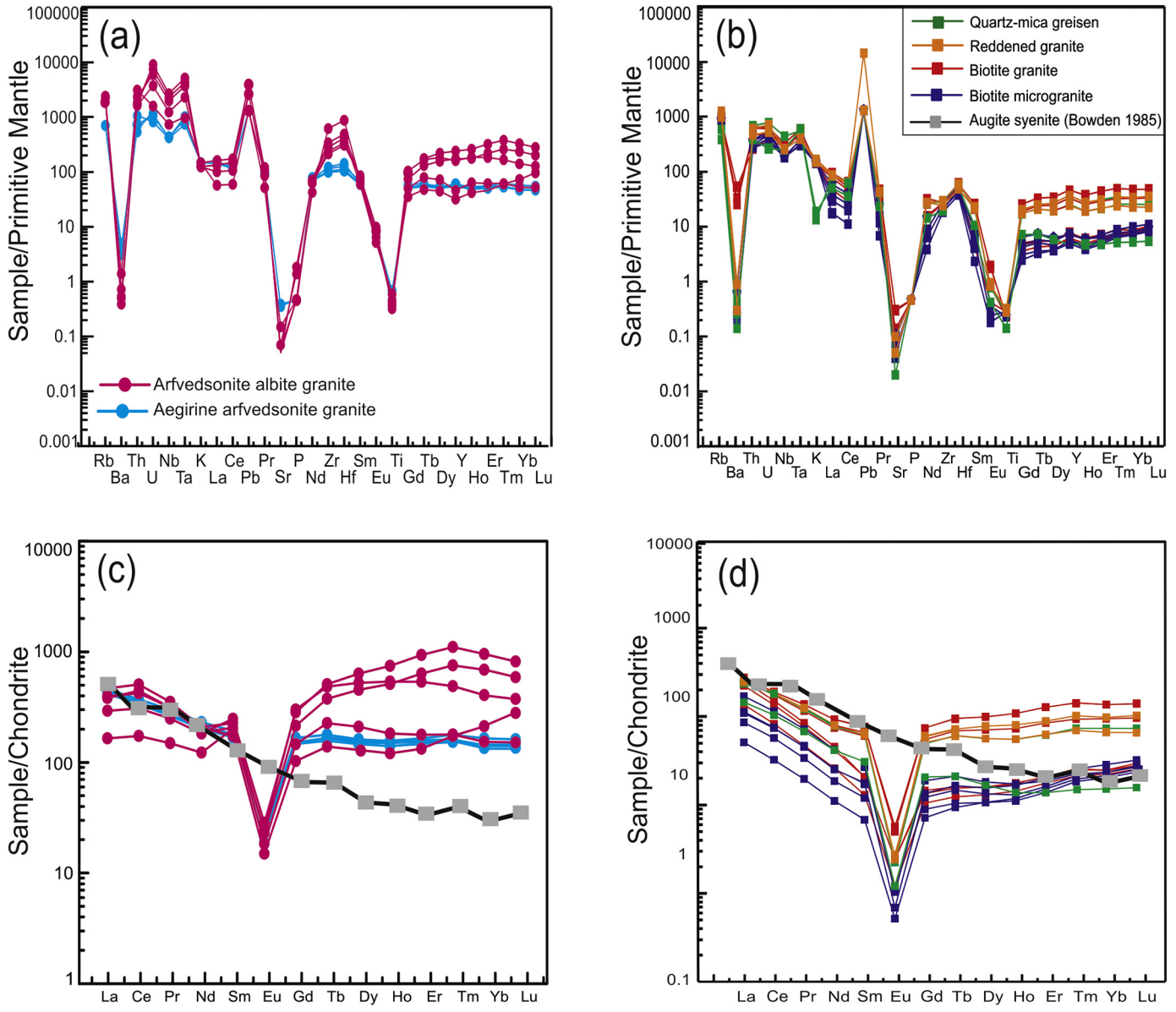

Fig. 6. (a-b) Primitive-mantle-normalized trace element spider diagrams and (c-d) chondrite-normalized REE distributions. Normalization factors used for the primitive-mantle-normalized spider diagram and chondrite-normalized REE diagram were taken from Sun and McDonough (1989) and Taylor and McLennan (1985), respectively.

upon primary albite, and it is closely associated with mafic minerals. Pyrochlore occurs as golden-yellow, high-relief isotropic octahedral crystals up to a millimetre in diameter.

The biotite granite is medium-grained, grey to yellowish in colour, and exhibits a relatively even, non-porphyritic texture (Fig. 3e). It is composed of orthoclase microperthite (50–55%), quartz (32–35%), albite (3.5 to 4.6%), and biotite (2–2.5%) (Fig. 3f). Quartz is mainly present as anhedral grains. Orthoclase microperthite is the dominant feldspar, but microcline occurs in small amounts. Carlsbad twinning is frequent, and perthite exhibits rare Baveno twinning. Edges of feldspar crystals are usually rimmed with narrow selvages of non-twinned secondary albite. Primary albite is small and occurs as well-twinned interstitial crystals between earlier minerals. Biotite is present as ragged highly pleochroic flakes, and is partially replaced by late-stage fluorite or albite with magnetite as an alteration by-product. Columbite is a primary minor constituent of the granite, and other accessory minerals include zircon, fluorite, and iron oxides (Fig. 3g-h).

Within the Liruei lode, the biotite granite has been extensively altered, giving rise to new textural and mineralogical assemblages accompanied by rare-metal (Sn–Nb–W) and sulphide (Pb—Zn) mineralization. The reddened wall rock, hereafter referred to as 'reddened granite', has a texture similar to that of the original biotite granite (Fig. 3i), but orthoclase microperthite has been completely replaced by poorly ordered secondary microcline (Fig. 3j). In addition, biotite is partially replaced by small clots of green mica. The alteration assemblages of the reddened granite grade inward into quartz-mica greisen characterized by complete breakdown of feldspars and development of green mica and fluorite (Fig. 3k-l).

4. Sampling and analytical methods

4.1. Sample collection

Twenty samples were collected in the Ririwai outcrops during a 3-day field expedition in January 2018. They include four representative samples of aegirine arfvedsonite granite, five of arfvedsonite albite granite, six of biotite granite, and five of biotite microgranite. In addition, two samples of reddened granite and two samples of quartz-

Table 2
LA-ICP-MS U—Pb isotope analytical results of zircons extracted from Ririwai A-type granites.

Samples/	Elements concen. (ppm)		Ratio	Isotopic ratios						Isotopic ages (Ma)					
Spot No.	Th	U	Th/U	$^{207}Pb/^{206}Pb$	1σ	$^{207}Pb/^{235}U$	1σ	$^{207}Pb/^{238}U$	1σ	$^{207}Pb/^{206}Pb$	1σ	$^{207}Pb/^{235}U$	1σ	$^{206}Pb/^{238}U$	1σ
Sample AZ1(Aegirine arfvedsonite granite)															
AZ1–02	64.5	84.4	0.8	0.0543	0.0153	0.2025	0.0493	0.0277	0.0012	383	537	187	42	176	7.5
AZ1–03	109.7	160.1	0.7	0.0545	0.0039	0.2074	0.0141	0.0278	0.0004	391	155	191	12	177	2.4
AZ1–07	85.9	137.5	0.6	0.0545	0.0055	0.2072	0.0196	0.0279	0.0007	394	228	191	16	177	4.4
AZ1–09	90.2	145.3	0.6	0.0516	0.0043	0.1894	0.0135	0.0268	0.0009	333	193	176	12	170	5.5
AZ1–11	91.1	148.9	0.6	0.0520	0.0048	0.2007	0.0168	0.0277	0.0005	287	211	186	14	176	3.3
AZ1–14	90.0	154.3	0.6	0.0493	0.0036	0.1865	0.0138	0.0277	0.0005	161	163	174	12	176	3.3
AZ1–16	110.7	158.2	0.7	0.0521	0.0069	0.2047	0.0257	0.0275	0.0007	287	278	189	22	175	4.2
AZ 1–23	2858.6	3479.7	0.8	0.0481	0.0016	0.1815	0.0053	0.0275	0.0003	105	77	169	5	175	2.2
AZ1–24	66.8	91.3	0.7	0.0501	0.0078	0.1919	0.0295	0.0278	0.0007	211	317	178	25	177	4.2
Sample KZ1(Arfvedsonite albite granite)															
KZ1–01	421.89	297.99	1.4	0.0474	0.0054	0.1935	0.0225	0.0295	0.0005	78	246	179	19	187	3.3
KZ1–05	807.90	115.70	7.0	0.0536	0.0062	0.2008	0.0258	0.0269	0.0008	354	258	186	22	171	4.7
KZ1–08	567.30	104.90	5.4	0.0521	0.0080	0.1882	0.0262	0.0265	0.0014	300	309	175	22	169	9.0
KZ1–11	737.50	93.60	7.9	0.0559	0.0096	0.2058	0.0317	0.0273	0.0013	450	389	190	27	174	8.0
KZ1–13	515.90	382.30	1.3	0.0517	0.0049	0.1930	0.0150	0.0273	0.0007	333	220	179	13	174	4.5
KZ1–25	452.60	112.50	4.0	0.0552	0.0045	0.2034	0.0155	0.0268	0.0006	420	181	188	13	171	4.0
Sample BZ2 (Biotite granite)															
BZ2–02	51.1	72.5	0.7	0.0559	0.0083	0.1998	0.0274	0.0266	0.0013	450	331	185	23	169	7.9
BZ2–03	270.2	526.8	0.5	0.0487	0.0045	0.1768	0.0171	0.0263	0.0005	132	213	165	15	167	3.1
BZ2–04	194.4	295.6	0.7	0.0549	0.0028	0.2095	0.0128	0.0276	0.0008	409	110	193	11	175	5.1
BZ2–05	51.7	81.0	0.6	0.0390	0.0088	0.1690	0.0267	0.0260	0.0008	398	160	159	23	166	5.2
BZ2–09	126.5	194.2	0.7	0.0543	0.0076	0.2014	0.0280	0.0270	0.0009	383	318	186	24	172	5.9
BZ2–12	115.7	115.6	1.0	0.0493	0.0061	0.1944	0.0187	0.0273	0.0007	161	267	180	16	174	4.3
BZ2–15	682.5	1148.9	0.6	0.0548	0.0024	0.2051	0.0086	0.0271	0.0003	406	96	189	7	173	2.1
BZ2–17	453.0	1066.6	0.4	0.0498	0.0016	0.1855	0.0063	0.0269	0.0003	187	74	173	5	171	2.2
BZ2–18	107.1	112.9	0.9	0.0508	0.0064	0.1915	0.0193	0.0273	0.0008	228	270	178	16	174	5.0
BZ2–20	175.3	268.2	0.7	0.0519	0.0082	0.1970	0.0292	0.0278	0.0007	280	326	183	25	177	4.5
BZ2–22	113.0	122.4	0.9	0.0511	0.0075	0.1885	0.0295	0.0263	0.0007	256	294	175	25	167	4.3
BZ2–23	54.6	86.9	0.6	0.0497	0.0069	0.1859	0.0230	0.0268	0.0007	189	291	173	20	170	4.4
BZ2–25	130.7	228.1	0.6	0.0505	0.0037	0.1851	0.0128	0.0269	0.0006	217	177	172	11	171	3.6
IBZ2–21*	241.8	248.1	1.0	0.0631	0.0025	0.8345	0.0303	0.0960	0.0011	722	83	616	17	590	6.8
Sample LZ1 (Biotite microgranite)															
L2–1-01	187.4	286.7	0.7	0.0492	0.0035	0.1750	0.0114	0.0263	0.0008	167	150	164	10	167	4.7
L2–1-03	119.8	185.3	0.6	0.0525	0.0037	0.1880	0.0124	0.0265	0.0005	306	131	175	11	168	3.0
L2–1-05	132.6	208.1	0.6	0.0489	0.0047	0.1803	0.0207	0.0260	0.0009	146	220	168	18	166	5.4
L2–1-06	208.1	358.1	0.6	0.0487	0.0039	0.1825	0.0156	0.0270	0.0007	200	122	170	13	172	4.3
L2–1-07	160.3	230.2	0.7	0.0545	0.0034	0.2011	0.0128	0.0267	0.0005	394	136	186	11	170	3.0
L2–1-08	174.9	315.7	0.6	0.0520	0.0045	0.1910	0.0155	0.0268	0.0005	283	197	177	13	170	3.1
L2–1-09	141.5	222.6	0.6	0.0518	0.0040	0.1907	0.0141	0.0271	0.0008	276	178	177	12	172	4.7
L2–1-10	162.1	309.7	0.5	0.0497	0.0032	0.1844	0.0111	0.0272	0.0006	183	145	172	10	173	3.6
L2–1-11	145.6	272.9	0.5	0.0507	0.0037	0.1840	0.0129	0.0264	0.0006	228	170	171	11	168	3.9
L2–1-12	238.3	455.9	0.5	0.0499	0.0028	0.1840	0.0099	0.0268	0.0006	191	131	172	9	170	3.5
L2–1-13	126.0	268.1	0.5	0.0489	0.0036	0.1783	0.0148	0.0263	0.0006	143	163	167	13	167	4.0
L2–1-14	136.7	217.6	0.6	0.0469	0.0059	0.1723	0.0207	0.0267	0.0009	56	265	161	18	170	5.4
L2–1-16	182.3	341.5	0.5	0.0523	0.0033	0.1936	0.0124	0.0270	0.0006	298	146	180	11	172	3.5
L2–1-17	242.5	484.4	0.5	0.0542	0.0033	0.2042	0.0142	0.0272	0.0006	389	144	189	12	173	3.8
L2–1-18	147.6	262.0	0.6	0.0549	0.0035	0.1971	0.0120	0.0263	0.0006	409	143	183	10	167	4.0
L2–1-20	253.5	498.7	0.5	0.0505	0.0027	0.1829	0.0089	0.0264	0.0004	217	122	171	8	168	2.6
L2–1-21	183.6	322.8	0.6	0.0541	0.0033	0.1998	0.0123	0.0268	0.0004	376	139	185	10	170	2.5
L2–1-22	294.6	525.2	0.6	0.0531	0.0039	0.1928	0.0146	0.0262	0.0005	345	169	179	12	167	2.9
L2–1-23	173.5	281.4	0.6	0.0504	0.0039	0.1903	0.0128	0.0266	0.0004	213	178	177	11	169	2.4
L2–1-24	163.6	286.9	0.6	0.0544	0.0029	0.2010	0.0106	0.0268	0.0004	391	119	186	9	171	2.5

mica greisen were collected. Due to poor accessibility, no samples of the granite porphyry could be collected. All 24 samples were analysed for their bulk-rock major and trace-element compositions, and subsets of eight samples were analysed for bulk-rock Sm—Nd isotopes. In addition, zircon grains were extracted from one sample of aegirine arfvedsonite granite, of arfvedsonite albite granite, of biotite granite, and of biotite microgranite for LA-ICP-MS U—Pb dating and Hf—Lu isotope analysis.

4.2. Whole-rock major- and trace-element analyses

Whole-rock major and trace element analyses were carried out at the ALS laboratory in Guangzhou, China. Prior to analysis, each sample was pulverized to finer than 200 mesh size using an agate ball mill. Major-element concentrations were analysed using an energy-dispersive X-ray fluorescence (XRF) spectrometer (Shimadzu EDX 700), with an analytical precision of <3%. The XRF analysis was carried out using pressed-powder discs with the international standard JG-2 as a reference. Trace elements and rare earth elements were analysed using an Agilent 7700e inductively coupled plasma-mass spectrometer (ICP-MS), with an analytical precision of ~5–10%. Prior to ICP-MS analysis, about 50 mg of each sample were dissolved in a combined lithium borate fusion and aqua regia digestion. International standard (JG-2) was used as reference materials.

4.3. LA-ICP-MS zircon U—Pb dating

Zircon grains were extracted from four samples (AZ1, BZ2, LZ1 and KZ1) using conventional heavy liquid and magnetic separation techniques. The zircon grains were handpicked under a binocular microscope, mounted in epoxy resin, and polished in order to expose the centre of each grain. Cathodoluminescence (CL) images of the zircon grains were captured at the State Key Laboratory of Geological Processes and Mineral Resources (GPMR), China University of Geosciences (Wuhan), using a scanning electron microscope (SEM) fitted with an energy-dispersive system (EDS).

U—Pb dating was carried out on an Analytik Jena PQMS Elite ICP-MS coupled with an ESI NWR 193-nm laser ablation system at GPMR. The analysis was conducted using helium as the carrier gas. The procedure involved a background acquisition time of 15 s (gas blank) followed by data acquisition at a 50-Hz frequency on a 44-μm ablation spot. Zircon 91,500 and glass NIST610 were used as external standards, and the ICP-MS-DataCal of Liu et al. (2010) was used for raw data selection, background integration, and time-drift correction. The Isoplot software of Ludwig (2003) was used to calculate mean weighted average (MSWD) ages and to generate concordia diagrams.

4.4. Zircon Lu—Hf isotope analysis

In-situ Lu—Hf isotope analysis was performed using a Neptune Plus MC-ICP-MS coupled with a Geolas 2005 Excimer ArF laser ablation system at GPMR. Each measurement was done for approximately 60 s with a laser power of 80 MJ/cm^2 on ablation spots adjacent to those for U—Pb age dating. Standard ratios of $^{176}Hf/^{175}Lu$ (0.02655) and $^{176}Yb/^{172}Yb$ (0.5886) were used to correct for isobaric interferences of ^{175}Lu on ^{176}Hf and ^{176}Yb on ^{176}Hf, respectively, as recommended by Machado and Simonetti (2001). Selection and integration of analytical signals and mass bias calibrations were carried out using the ICP-MS-DataCal of Liu et al. (2010). For epsilon Hf (εHf(t)) computations, we used the recommended present-day chondritic ratios of $^{176}Hf/^{177}Hf$ (0.282772) and $^{176}Lu/^{177}Hf$ (0.0332) of Belousova et al. (2006). Single-stage Hf model ages (T^1_{MD}) were calculated using the present-day depleted mantle ratios of $^{176}Hf/^{177}Hf$ (0.28325) and $^{176}Lu/^{177}Hf$ (0.0384) of Griffin et al. (2002). Crustal Hf model ages (T^C_{DM}) were computed using the mean continental crust $^{176}Lu/^{177}Hf$ ratio (0.015) of Belousova et al. (2006).

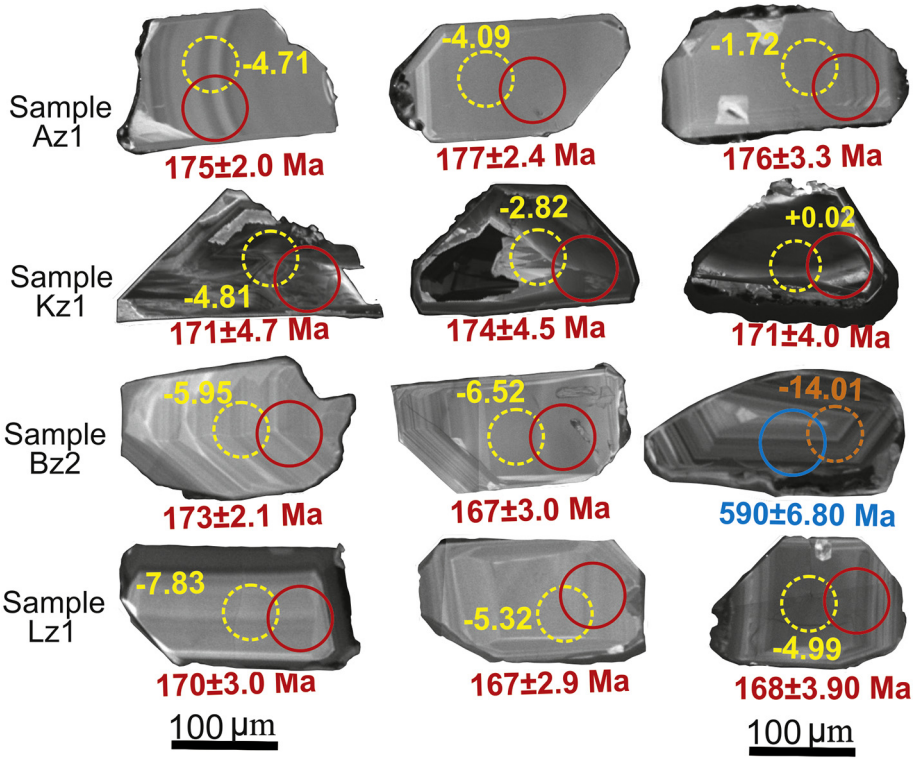

Fig. 7. Cathodoluminescence (CL) images of representative zircon crystals from the Ririwai peralkaline and aluminous A-type granites analysed for U—Pb age and Lu—Hf isotopes. Samples: AZ1 (aegirine arfvedsonite granite), KZ1 (arfvedsonite albite granite), BZ2 (biotite granite) and LZ1 (biotite microgranite). Red circles indicate LA-ICP-MS analytical spots for U—Pb dating; yellow circles indicate Lu—Hf isotope analytical spots; blue and orange circles indicate LA-ICP-MS analytical spots for U—Pb and Lu—Hf isotopes, respectively, in the inherited zircon of sample BZ2.

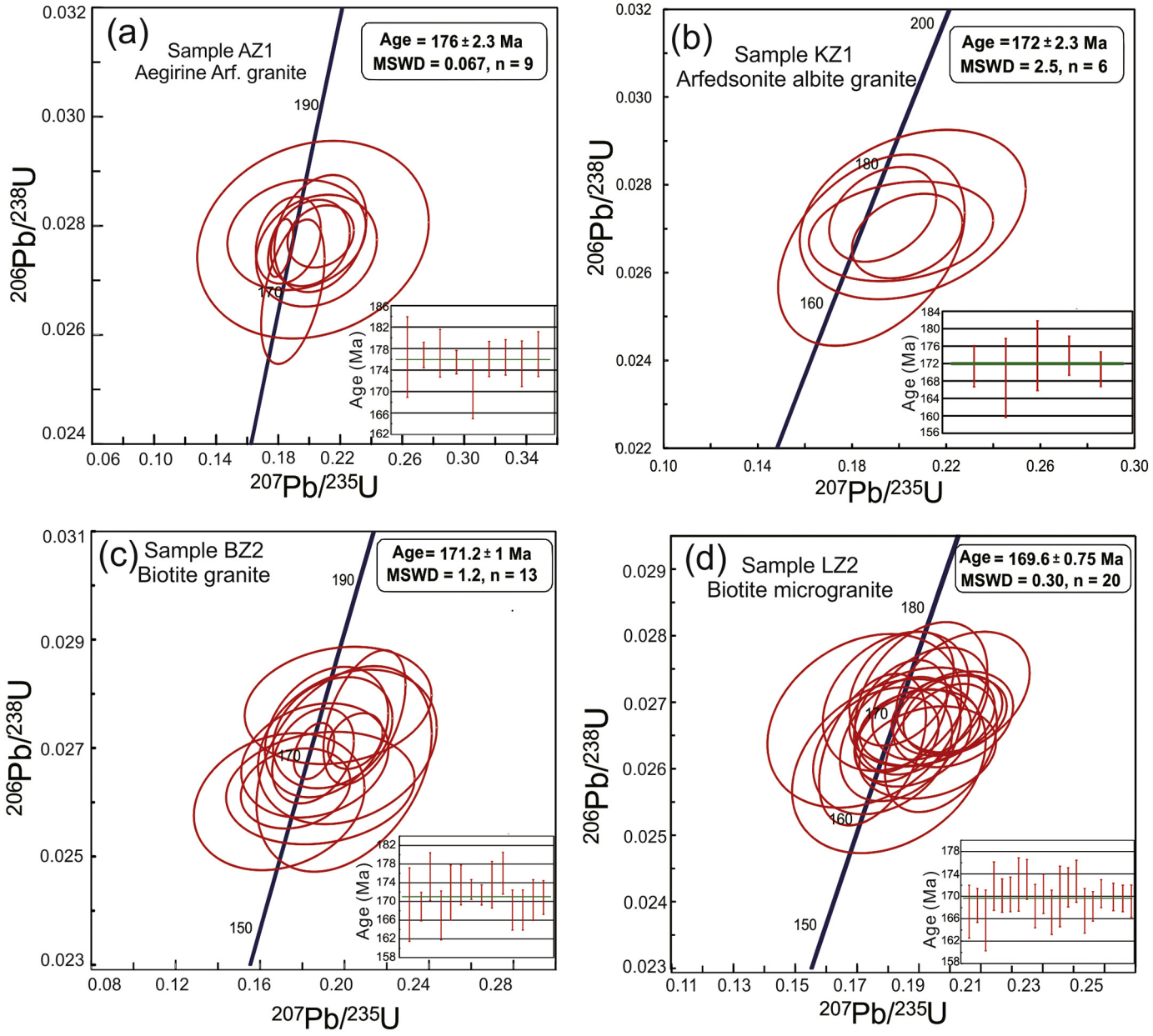

Fig. 8. LA-ICP-MS zircon U—Pb age concordia plots.

4.5. Whole-rock Nd isotope analysis

Whole-rock Nd isotope analysis was performed using a Micromass Isoprobe Multi-Collector Inductively Coupled Plasma Mass Spectrometer (MC-ICP-MS) at the ALS Laboratory in Guangzhou, China. About 50–100 mg of powdered sample was digested in a distilled HF-HNO_3 solution in screw-top PFA beakers at a minimum temperature of 120 °C for 15 days prior to the isotopic measurement. Nd was then separated from the other REEs using a Di-(2-ethylhexyl) phosphoric acid (HDEHP) column. Samples were alternated with the JNdi-1 standard ($^{143}Nd/^{144}Nd = 0.512109 \pm 12$; 2σ), and measured $^{143}Nd/^{144}Nd$ values were corrected to $^{146}Nd/^{144}Nd = 0.7219$, as recommended by Li and McCulloch (1998). A single-stage neodymium model age was computed assuming linear neodymium isotopic growth from a depleted mantle reservoir with $\varepsilon Nd = 0$ at $t = 4.56$ Ga to $\varepsilon Nd = +10$ at present, and a two-stage model age was calculated assuming that the protoliths of the granitic magmas had a fSm/Nd value or Sm/Nd ratio equal to that of average continental crust (e.g., Jahn et al., 2001).

5. Results

5.1. Major and trace element compositions

The major and trace element compositions of the 24 samples are listed in Table 1. With the exception of quartz-mica greisen, which has exceedingly high SiO_2 concentrations (91.33–93.09 wt%) and low alkalis (0.45 to 0.61 wt%), samples yield SiO_2 contents ranging from 70.71 to 77.49 wt% and high total alkali contents ($Na_2O + K_2O$, 7.76 to 11.37 wt %). They plot in the granite field according to the classification of Le Maitre (1989; Fig. 4a), but two samples of arfvedsonite albite granite fall in the field of quartz syenite in the cationic diagram of De La Roche et al. (1980) (Fig. 4b). Depending on molar $Al_2O_3/(Na_2O + K_2O)$ (= A/NK) ratios, they are either peralkaline (A/NK < 1.00), or metaluminous to peraluminous (A/NK > 1.00) (Fig. 4c). All samples are poor in CaO (0.02 to 0.35 wt%), MgO (0.01 to 0.04 wt%), P_2O_5 (0.01 to 0.04 wt%), and TiO_2 (0.03 to 0.1 wt%), and yield moderate to high $Fe_2O_3^T$ (1.62 to 4.49 wt%) and Al_2O_3 (10.96 to 13.98 wt%). They

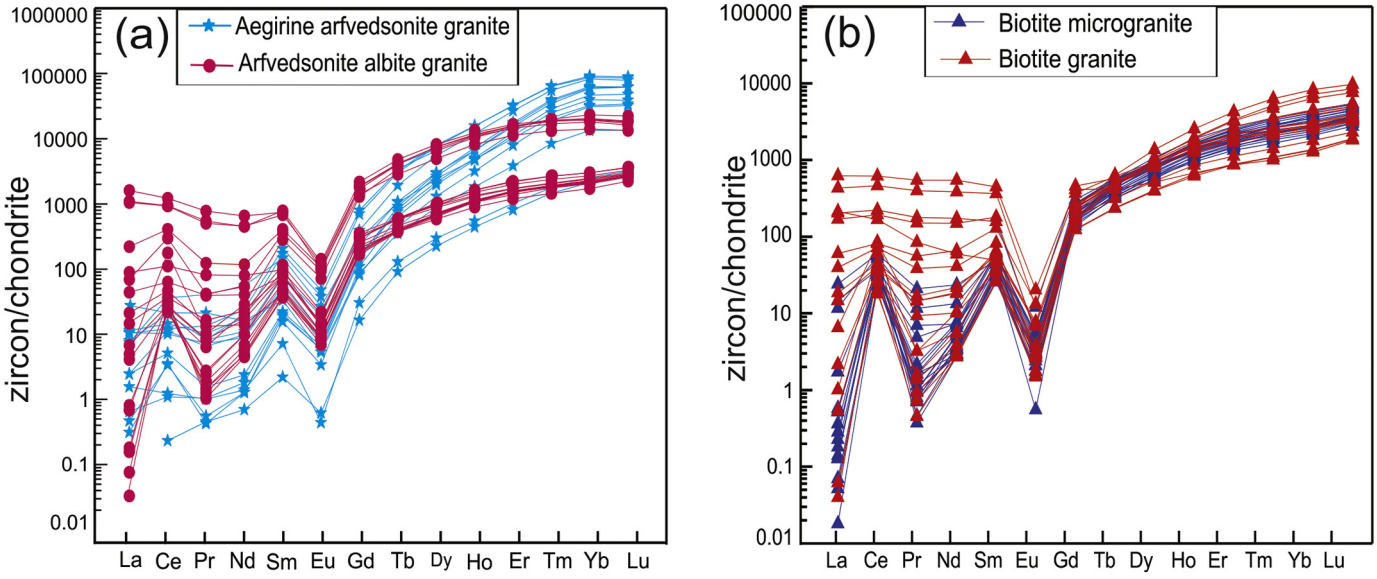

Fig. 9. Chondrite-normalized REE plots for (a) peralkaline granit.es; (b) aluminous granite. Normalization values were taken from Taylor and McLennan (1985).

plot within the field of high-K granites in the K_2O vs. SiO_2 diagram (Fig. 4d) and exhibit $K_2O > Na_2O$, with the exception of arfvedsonite albite granite, which yields very high Na_2O concentrations owing to late-stage albitization.

Aegirine arfvedsonite granite is mildly peralkaline, with 1.12 to 1.20 wt% CIPW-normative acmite and peralkaline index (molar $Al_2O_3/(Na_2O + K_2O)$) of 1.02 to 1.03. Arfvedsonite albite granite is strongly peralkaline with 0.99 to 1.26 wt% CIPW-normative acmite corresponding to peralkaline index of 1.15 to 1.23. The granite porphyry is also mildly peralkaline (peralkaline index = 0.91–1.05, Kinnaird et al., 1985).

Although biotite granite has similar alkali contents to aegirine arfvedsonite granite (Table 1), it is metaluminous to mildly peraluminous, due to slightly higher Al_2O_3 contents. Reddened granite yields higher values of the alumina saturation index (A/CNK = molar $Al_2O_3/(CaO + Na_2O + K_2O)$; average = 1.07) than the original biotite granite (average A/CNK = 1.02). Biotite microgranite plots right within the peraluminous field (Fig. 4d), A/CNK values ranging from 1.08 to 1.32 (average = 1.17), corresponding to CIPW-normative corundum ranging from 0.98 to 3.10 (average = 1.77).

Major oxides show considerable variations, with increasing silica (SiO_2). The peralkaline granites have generally higher TiO_2 and similar K_2O contents than the aluminous (metaluminous to peraluminous) granites (Fig. 5a-f). Because the concentrations of MgO and P_2O_5 are generally low (<0.05 wt%) in all the granites, they are not plotted in Fig. 5.

The peralkaline granites have higher amounts of Nb (291 to 1915 ppm), Zr (1100 to 6940 ppm), Hf (31.9 to 272 ppm), U (17.2 to 190 ppm), and ΣREE (584 to 1053 ppm) than the aluminous granites (Nb = 128 to 234 ppm, Zr = 214 to 332 ppm, Hf = 11.7 to 19.4 ppm, U = 5.6 to 16.4 ppm, and ΣREE = 53 to 354 ppm) contents. Primitive mantle-normalized values of some LILE (Rb, Th, U), LREE (La, Ce, Nd) and HFSE (Zr, Hf) in the peralkaline granites, especially the arfvedsonite albite granite, are higher than in the aluminous granites (Fig. 6a, b). Chondrite-normalized REE patterns in the highly altered peralkaline arfvedsonite albite granite show preferential enrichment of HREE relative to LREE, along with an "M-type" La—Nd tetrad effect (a convex-up pattern characterized by high Ce but low La and Nd; Fig. 6c). The mildly peralkaline aegirine arfvedsonite granite and the aluminous granites show enriched LREE and HREE patterns compared to augite syenite, considered representative of parental magma by Bowden (1985) and Kinnaird et al. (1985) (Fig. 6c, d). All Ririwai samples are marked by deep negative Eu anomalies suggesting significant feldspar fractionation (Fig. 6c, d).

Zircon saturation temperatures, computed using the model of Watson and Harrison (1983) are generally high, but higher for the peralkaline granites (~1000 °C) than for the aluminous granites (~850 °C). However, calculated temperatures are likely overestimated and may represent maximum values based on two lines of evidence: (i) Zr is highly soluble in peralkaline felsic melts, compared to the metaluminous felsic melts on which the saturation model is based, and (ii) the inherited zircon crystals found in biotite granite (see below) suggest that a potentially significant fraction of Zr may be stored in xenocrysts in addition to the melt.

5.2. Zircon U—Pb ages

Analytical results of LA-ICP-MS U—Pb zircon dating grains are listed in Table 2. Most crystals are euhedral to subhedral, ranging in colour from light brown to pale yellow and in size from 100 to 200 μm with length/width ratios of 1:1 to 2:1 (Fig. 7). Although most of the zircons exhibit magmatic textures (e.g., oscillatory zoning), some zircons from the albite-arfvedsonite granites and biotite granites do not show simple magmatic zonation, suggesting more than one period of crystallization.

The zircon grains extracted from the aegirine arfvedsonite granite (sample AZ1) show oscillatory zoning and yielded Th/U ratios ranging from 0.6 to 0.8, typical of magmatic zircon (Belousova et al., 2002). Eight concordant crystals with low degrees of discordance (< 8%) yield $^{206}Pb/^{238}U$ age clusters between 177 and 175 Ma, with a weighted mean age of 176 ± 2.3 Ma (MSWD = 0.067) (Fig. 8a), close to the whole-rock Rb—Sr age of 175 ± 5 Ma (Toarcian, Early Jurassic) (Van Breemen et al., 1975), although a younger age of 168 ± 6 Ma (Middle Jurassic) was reported by Dickin et al. (1991). A single concordant crystal yields a lower $^{206}Pb/^{238}U$ age of 170 ± 5.5 Ma, suggesting isotopic disturbance by hydrothermal fluids.

In contrast, zircon grains of the arfvedsonite albite granite (sample KZ1) have Th (452.6 to 2468 ppm) in excess of U (76.4 to 636.9 ppm) with high Th/U ratios (1.3 to 7.9). They crystallized during the late-magmatic stage, concurrently with U-bearing pyrochlore (e.g., Ogunleye et al., 2006). Chondrite-normalized patterns show strong LREE enrichment by up to 1000× relative to LREE in unaltered zircon (Fig. 9a). Crystals with high degrees of discordance (n = 9) were rejected and are not listed in Table 2. Five clustered crystals show low degrees of discordance (< 10%) and yield a weighted mean $^{206}Pb/^{238}U$

Table 3
Zircon Lu—Hf isotope compositions of zircons extracted from Ririwai A-type granites.
Note: LBZ2 21*is an inherited zircon,

Spot No.	$^{176}Yb/^{177}Hf$	$^{176}Lu/^{177}Hf$	$^{176}Hf/^{177}Hf$	$\pm 2\sigma$	εHf(t)	T_{DM}(Ma)	T^{c}_{DM}(Ma)	$f_{Lu/Hf}$
Sample AZ1 (Aegirine arfvedsonite granite)								
AZ1–2	0.0383	0.0011	0.2825	0.00002	−4.7	1019	1520	−0.97
AZ1–3	0.0410	0.0011	0.2826	0.00003	−4.09	991	1477	−0.97
AZ1–7	0.0573	0.0016	0.2826	0.00005	−3.81	995	1463	−0.95
AZ1–9	0.0376	0.0010	0.2825	0.00003	−5.8	1056	1585	−0.97
AZ1–11	0.0349	0.0009	0.2825	0.00003	−5.1	1028	1543	−0.97
AZ1–14	0.0488	0.0014	0.2826	0.00006	−1.72	905	1329	−0.96
AZ1–16	0.3120	0.0072	0.2826	0.00003	−2.32	1066	1365	−0.78
AZ1–23	0.0561	0.0015	0.2825	0.00003	−4.71	1027	1519	−0.96
AZ1–24	0.0374	0.0010	0.2826	0.00002	−3.16	955	1420	−0.97
Sample KZ1 (Arfvedsonite albite granite)								
KZ1–1	0.2614	0.0070	0.2826	0.000028	−1.92	1047	1344	−0.79
KZ1–5	0.0298	0.0007	0.2825	0.000014	−4.81	1023	1535	−0.98
KZ1–8	0.9546	0.0245	0.2827	0.000063	−1.36	2059	1295	−0.26
KZ1–11	1.3918	0.0334	0.2829	0.000082	5.31	3424	875	0.01
KZ1–13	0.0197	0.0005	0.2826	0.000014	−2.82	935	1403	−0.98
KZ1–25	0.3909	0.0103	0.2827	0.000038	0.02	1054	1227	−0.69
Sample BZ2 (Biotite granite)								
BZ2–3	0.0681	0.0022	0.2825	0.00003	−6.52	1112	1630	−0.94
BZ2–4	0.0471	0.0013	0.2825	0.000016	−6.14	1075	1605	−0.96
BZ2–9	0.0460	0.0013	0.2825	0.000019	−5.45	1049	1564	−0.96
BZ2–12	0.0418	0.0012	0.2825	0.000026	−5.62	1056	1576	−0.96
BZ2–15	0.0330	0.0010	0.2825	0.000021	−6.73	1086	1639	−0.97
BZ2–17	0.0743	0.0022	0.2825	0.000015	−5.3	1066	1554	−0.93
BZ2–22	0.0384	0.0011	0.2825	0.000025	−5.88	1059	1588	−0.97
BZ2–23	0.0188	0.0006	0.2825	0.000019	−5.42	1030	1561	−0.98
BZ2–25	0.0581	0.0018	0.2826	0.000033	−2.35	935	1366	−0.94
IBZ2–21*	0.0341	0.0010	0.2820	0.00002	−14.01	1717	2402	−0.97
Sample LZ1 (Biotite microgranite)								
LZ1–3	0.0304	0.0009	0.2825	0.000024	−7.6	1125	1700	−0.97
LZ1–6	0.0521	0.0013	0.2826	0.000021	−4.25	998	1483	−0.96
LZ1–7	0.0542	0.0016	0.2825	0.000031	−7.83	1153	1714	−0.95
LZ1–9	0.0406	0.0011	0.2825	0.00002	−7.01	1110	1665	−0.97
LZ1–10	0.0441	0.0013	0.2825	0.000033	−7.21	1123	1677	−0.96
LZ1–11	0.0334	0.0009	0.2825	0.000022	−4.99	1022	1534	−0.97
LZ1–12	0.0494	0.0014	0.2824	0.000017	−7.82	1150	1717	−0.96
LZ1–13	0.0392	0.0011	0.2825	0.000018	−4.93	1027	1533	−0.97
LZ1–15	0.0390	0.0011	0.2825	0.000025	−5.95	1067	1598	−0.97
LZ1–18	0.0360	0.0010	0.2826	0.000024	−4.08	991	1479	−0.97
LZ1–20	0.0453	0.0013	0.2825	0.000018	−7.02	1113	1665	−0.96
LZ1–22	0.0466	0.0013	0.2825	0.000017	−5.32	1047	1557	−0.96

age of 172 ± 2.3 Ma (MSWD = 1.8) (Fig. 8b), roughly similar to the whole rock Rb—Sr age of 176 ± 5 Ma (Van Breemen et al., 1975), although a younger age of 166 ± 7 Ma was reported by Dickin et al. (1991). One concordant crystal yields a slightly older age of 187 ± 3.3 Ma, similar to whole rock Rb—Sr age of the neighbour Ninji Burra nested complex (Rahaman et al., 1984).

Zircon grains of the biotite granite (sample BZ2) show oscillatory zoning and have magmatic Th/U ratios (0.4 to 1). Chondrite-normalized patterns show varying Ce positive anomalies and deep Eu negative anomalies (Fig. 9b). Thirteen crystals with high degrees of concordance (> 90%) yield a weighted mean $^{206}Pb/^{238}U$ age of 171.2 ± 1 Ma (MSWD = 1.2) (Fig. 8c), identical to the whole rock Rb—Sr age of 171 ± 2 Ma (Aalenian, early Middle Jurassic) (Van Breemen et al., 1975), although a younger age of 165.8 ± 1.6 Ma was reported by Dickin et al. (1991). One crystal with a distinctive morphology (length/width ratios of 3:1) (Fig. 7) yields a $^{206}Pb/^{238}U$ age of 590 ± 6.75 Ma (Ediacaran), within the range of Pan-African post-collisional granites, and is interpreted as inherited. Altered crystals with no visible oscillatory zoning, low Th/U ratios (< 0.2) and high LREE contents, and crystals with high common Pb were excluded from the calculation and are not listed in Table 2.

Zircon grains of the biotite microgranite (n = 20) mostly show oscillatory zoning and have high magmatic Th/U values (0.5 to 0.7). Twenty concordant crystals yield $^{206}Pb/^{238}U$ ages ranging from 167 to 173 Ma, with a weighted mean age of 169.6 ± 0.75 Ma (MSWD = 0.30) (Bajocian, Middle Jurassic) (Fig. 8d). In a chondrite-normalized diagram, their REE patterns, with pronounced Ce positive and Eu negative anomalies, are similar to zircon of the biotite granite (Fig. 9b).

The emplacement of Ririwai plutonic rocks took place around the Early-Middle Jurassic boundary, during a ~5-Myr interval from the Toarcian to the Aalenian in the case of the peralkaline granites and during <2 Myr from the Aalenian to the Bajocian in the case of the aluminous granites, which is in agreement with the intrusive sequence observed in the field.

5.3. Zircon Lu—Hf isotopes

Zircon Lu—Hf isotope compositions are listed in Table 3. Nine grains of aegirine arfvedsonite granites, including the 170-Ma crystal, yield $^{176}Hf/^{177}Hf$ ratios ranging from 0.2824 to 0.2826 and calculated εHf (t) from −5.10 to −1.72, corresponding to Paleoproterozoic crustal model (T^C_{DM}) ages from 1585 Ma to 1329 Ma.

Seven zircon grains of arfvedsonite albite granite (n = 8) yield $^{176}Hf/^{177}Hf$ ratios from 0.2825 to 0.2829 and εHf(t) values from −4.81 to +5.31, corresponding to Mesoproterozoic crustal model ages from 1535 Ma to 832 Ma. Two altered crystals, characterized by high $^{176}Yb/^{177}Hf$ (> 0.8) and $^{176}Lu/^{177}Hf$ (> 0.002) ratios (Table 3), yield the highest εHf(t) values and the lowest crustal model ages, suggesting that their Lu—Hf isotopic composition was modified during late-stage albitization (e.g., Ogunleye et al., 2006). The 187-Ma crystal yields εHf (t) of −1.92 and T^C_{DM} of 1344 Ma, in the same range of the other crystals.

Nine zircon grains of biotite granite (n = 9) yield $^{176}Hf/^{177}Hf$ ratios from 0.2824 to 0.2826 and εHf(t) values from −6.73 to −2.35, corresponding to Mesoproterozoic crustal model ages of 1639 Ma to 1366 Ma. The inherited Pan-African-aged crystal yields a low $^{176}Hf/^{177}Hf$ ratio of 0.2820 and an εHf(t) value of −14.01, corresponding to a T^C_{DM} age of 2402 Ma (Early Paleoproterozoic).

Twelve zircon grains of biotite microgranite (n = 12) yield $^{176}Hf/^{177}Hf$ ratios from 0.2824 to 0.2825 and εHf(t) values from −7.83 to −4.08, corresponding to Mesoproterozoic crustal model ages from 1717 Ma to 1479 Ma.

5.4. Whole-rock Sm—Nd isotopes

Whole-rock Sm—Nd isotope data are listed in Table 4. The peralkaline granites have Sm and Nd concentrations of 25.9–38.0 ppm

Table 4
Sm—Nd isotope compositions of A-type granites of Ririwai complex.

Samplea no.	Sm	Nd	Sm/Nd	$^{147}Sm/^{144}Nd$	$^{143}Nd/^{144}Nd$	±2σ	*f*Sm/Nd	εNd (t)	T_{DM1} (Ma)	T_{DM2} (Ma)
AZ1	29.7	108	0.275	0.1662	0.5125	4.0	−0.15	−1.92	2074	1116
A4	25.9	97.8	0.2648	0.1601	0.5125	5.0	−0.19	−2.1	1883	1131
KZ1	38	85.3	0.4455	0.2693	0.5126	4.0	0.36	−2.28	−1520	1160
K13	31.3	87.1	0.3594	0.2172	0.5126	4.0	0.1	−1.2	−2614	1060
BZ2	11.8	43.4	0.2719	0.1644	0.5124	5.0	−0.16	−3.55	2251	1240
B1	11.7	43.6	0.2672	0.1615	0.5124	4.0	−0.18	−3.51	2133	1238
LZ1	2.6	12.0	0.2183	0.1320	0.5124	6.0	−0.33	−3.26	1402	1222
L3	1.8	8.7	0.2115	0.1279	0.5124	8.0	−0.35	−3.34	1351	1229

T_{DM1} = single-stage model age, computed by assuming a linear Nd isotopic growth involving a depleted mantle reservoir.
T_{DM2} = two-stage model stage, computed by assuming that the *f*Sm/Nd of granitic protolith is equal to that of the average. Continental crust.

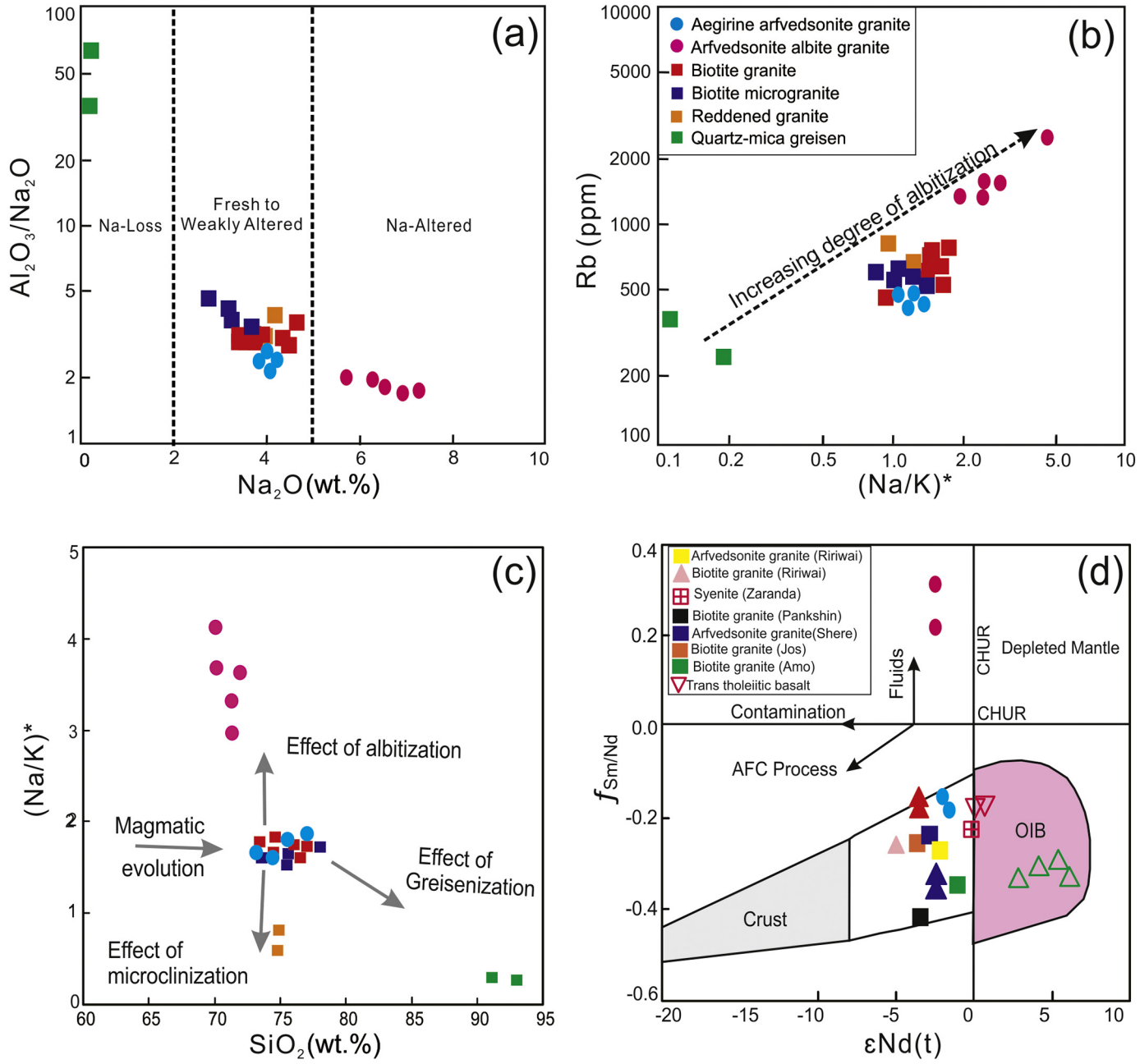

Fig. 10. Discriminant plots showing the effect of late-magmatic fluids on the Ririwai A-type granites. (a) Al_2O_3/Na_2O vs. Na_2O (after Spitz and Darling, 1978), (b) Rb vs. (Na/K)* (in cations) (after Kaur et al., 2012), (c) (Na/K)* vs. SiO_2, and (d) $f_{Sm/Nd}$ vs. εNd(t) plots.

and 85.3–108 ppm, respectively. The aluminous granites have lower Sm and Nd concentrations of 1.8–11.8 ppm and 8.7–43.6 ppm, respectively. Likewise, the peralkaline granites yield higher $^{147}Sm/^{144}Nd$ ratios (0.1601–0.2693) than the aluminous granites (0.1279–0.1644). All granites have $^{147}Sm/^{144}Nd$ ratios higher than the CHUR value of 0.1967 (Table 4), whereas two samples of arfvedsonite albite granite have $^{147}Sm/^{144}Nd$ ratios higher than the DM value of 0.2137.

Values of εNd(t), T_{DM1} and T_{DM2} model ages were computed with "t" corresponding to the zircon U—Pb ages of the granites. Calculated εNd(t) range from −2.28 to −1.20 for the peralkaline granites and from −3.55 to −3.26 for the aluminous granites, within the range from −5.6 to +0.9 reported for five other syenite-granite complexes in the Jos Plateau (Dickin et al., 1991). Except the arfvedsonite albite granite yielding positive $f_{Sm/Nd}$ values of +0.1 and + 0.37, the other granites yield negative $f_{Sm/Nd}$ values from −0.35 to −0.15. As $^{147}Sm/^{144}Nd$ ratios are very high in the peralkaline granites and the biotite granites (all >0.15), T_{DM1} and T_{DM2} model ages are meaningless. The biotite microgranites, with the lowest $^{147}Sm/^{144}Nd$ ratios of 0.1320 and 0.1279, yield Mesoproterozoic T_{DM2} ages of 1222 Ma and 1229 Ma.

6. Discussion

The present Ririwai ring complex contains largely unaltered volcanics and granites as well as granites that have been hydrothermally altered to varying degrees. To unravel their magmatic and hydrothermal histories, whole-rock major and trace element, Sm—Nd isotope, and zircon Hf isotope data offer useful information on the successive processes that have affected these granites.

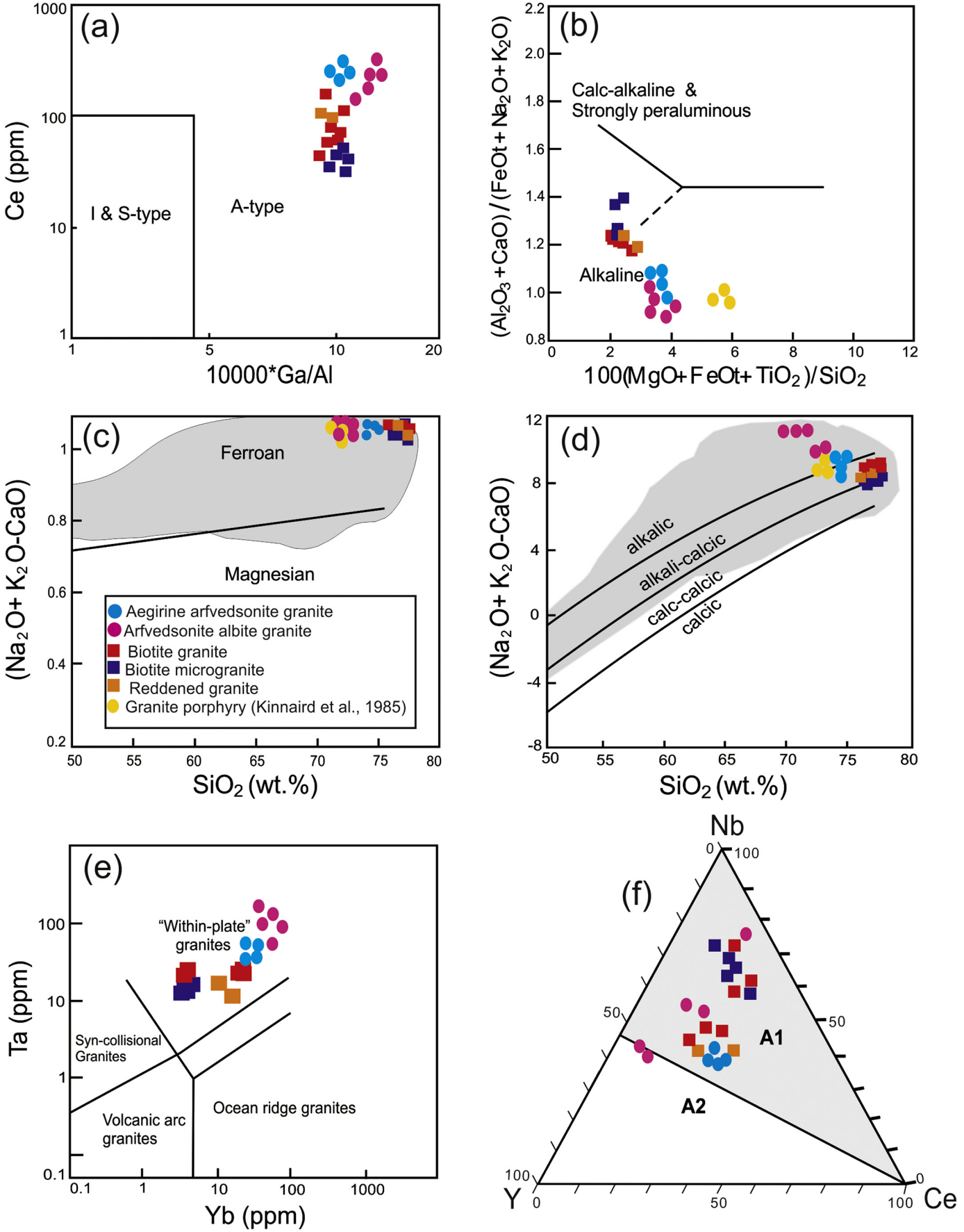

Fig. 11. Discriminant plots for the Ririwai A-type granites. (a) 10,000 × Ga/Al vs. Ce, (b) 100 × (MgO + FeOt + TiO_2)/SiO_2 vs. (Al_2O_3 + CaO)/(FeOt + Na_2O + K_2O), (c) SiO_2 vs. FeOt/(FeOt + MgO), (d) SiO_2 vs. (Na_2O + K_2O – CaO), (e) Yb vs. Ta, (f) Nb-Y-Ce diagram, (a) after Whalen et al. (1987), (b) after Sylvester (1989), (c) and (d) after Frost and Frost (2001), (e) after Pearce et al. (1984), and (f) after Eby (1992).

6.1. Effects of late-stage fluids

The Ririwai A-type granites experienced multi-stage sub-solidus hydrothermal fluid reactions, which caused mineralogical and chemical changes in the affected granites. Hydrothermal processes started with sodic metasomatism (albitization) following the exsolution of fluorine-bearing fluids during the late magmatic stage (cf. Ogunleye et al., 2006). This exsolution (melt-fluid unmixing) event caused a slight LREE/HREE decoupling due to preferential accumulation of LREE in the high-temperature fluorine-bearing fluids (e.g., Migdisov et al., 2016). Consequently, hydrothermally-altered zircons in the albitized arfvedsonite albite granite and biotite granite show LREE enrichment by up to 1000× relative to LREEs in unaltered zircons. In addition, albitization also resulted in pervasive replacement of orthoclase mesoperthite by secondary albite and modification of LILE (Rb and Sr) distributions in the affected rock, as shown by the positive correlation of Rb with the albitization index (Na/K ratio) (Fig. 10a).

LREE/HREE decoupling in the arfvedsonite albite granite may have resulted in disturbance of the Sm—Nd isotopic system, as evidenced by decoupling of *f*Sm/Nd and εNd(t) (Table 4). Samples with negative εNd(t) are expected to yield negative *f*Sm/Nd. Positive *f*Sm/Nd in the arfvedsonite albite granite, despite negative εNd(t) (Fig. 10d), is evidence of fluid-induced Sm—Nd isotopic disturbance (cf. Gysi et al., 2016). Moreover, altered zircons in the arfvedsonite albite granite yield high $^{176}Lu/^{177}Hf$ ratios (>0.002) and positive εHf(t), compared to unaltered zircons with low $^{176}Lu/^{177}Hf$ ratios (≤0.002) and negative εHf(t). Positive εHf(t) values in the altered zircons do not reflect εHf (t) magmatic signatures, but they may indicate fluid-induced Lu—Hf isotopic disturbance.

While albitization was most intense in the peralkaline granites, additional metasomatic processes including microclinization and greisenization affected the aluminous granites (Fig. 10c). Potash metasomatism (microclinization) led to replacement of orthoclase microperthite by deuteric microcline, as well as partial replacement of biotite with small clots of green mica (ferrous siderophyllite?). This process resulted in slight increases in the concentrations of $Fe_2O_3^T$, K_2O, and Rb in the affected samples (reddened granite) relative to the unaltered biotite granite (Table 1). In contrast, greisenization (acid metasomatism) caused complete destabilization of feldspars and the formation of secondary mica assemblages with compositions ranging from annite to siderophyllite (Kinnaird et al., 1985; Fig. 3k-l). This process led to the formation of quartz-mica greisen, which is characterized by a high content of normative quartz but low contents of total alkalis ($Na_2O + K_2O < 1$) and feldspar-compatible trace elements such Sr and Ba (Table 1).

6.2. Granite classification and tectonic affinity

The Ririwai peralkaline and aluminous granites are A-type granites, as shown by marked enrichments of Rb, Nb, Ga, and REE (except Eu) and strong depletions of Sr and Ba (Bonin, 2007; Whalen et al., 1987). Compared to typical I-type granite, the Ririwai granites are depleted in CaO, MgO and P_2O_5 and have higher alkali oxides ($Na_2O + K_2O$) and Ga/Al ratios. According to the Frost et al. (2001) classification, peralkaline granites are strongly ferroan and alkalic, whereas aluminous granites are strongly ferroan and alkali-calcic (Fig. 11c, d). The Ririwai granites plot (i) within the field of A-type granites in the Ce vs. 10,000 Ga/Al discrimination diagram (Fig. 11a), (ii) within the alkaline granite field, which distinguishes them from calc-alkaline I-type granites, in the Sylvester (1989) discrimination diagram (Fig. 11b), and (iii) in the field of within-plate granites in the Pearce et al. (1984) discrimination diagrams (Fig. 11e). Finally, in Nb-Y-Ce ternary plots (Eby, 1992), the Ririwai granites plot within the A1 field (Fig. 11f), with the exception of two samples of arfvedsonite albite granite that plot within the A2 field and have more Y and less Nb than the other samples.

6.3. Petrogenesis

6.3.1. Magma source

Our combined elemental, whole-rock Sm—Nd isotope, and zircon Hf isotope data enabled constraints to be placed on the most likely magma sources for the Ririwai A-type suite. These granites yield fairly high but negative εNd(t) values, i.e., −2.28 to −1.20 for the peralkaline granites and −3.55 to −3.26 for the aluminous granites. Thus, Pan-African and Paleoproterozoic basement rocks, which at 172 Ma had εNd(t) values of −10.38 to −20.49 (Dada et al., 1995) and −11.72 to −26.87 (Dickin et al., 1991), respectively, cannot have been the sole sources of their magmas. Even the Pan-African fayalite-bearing quartz-monzonite

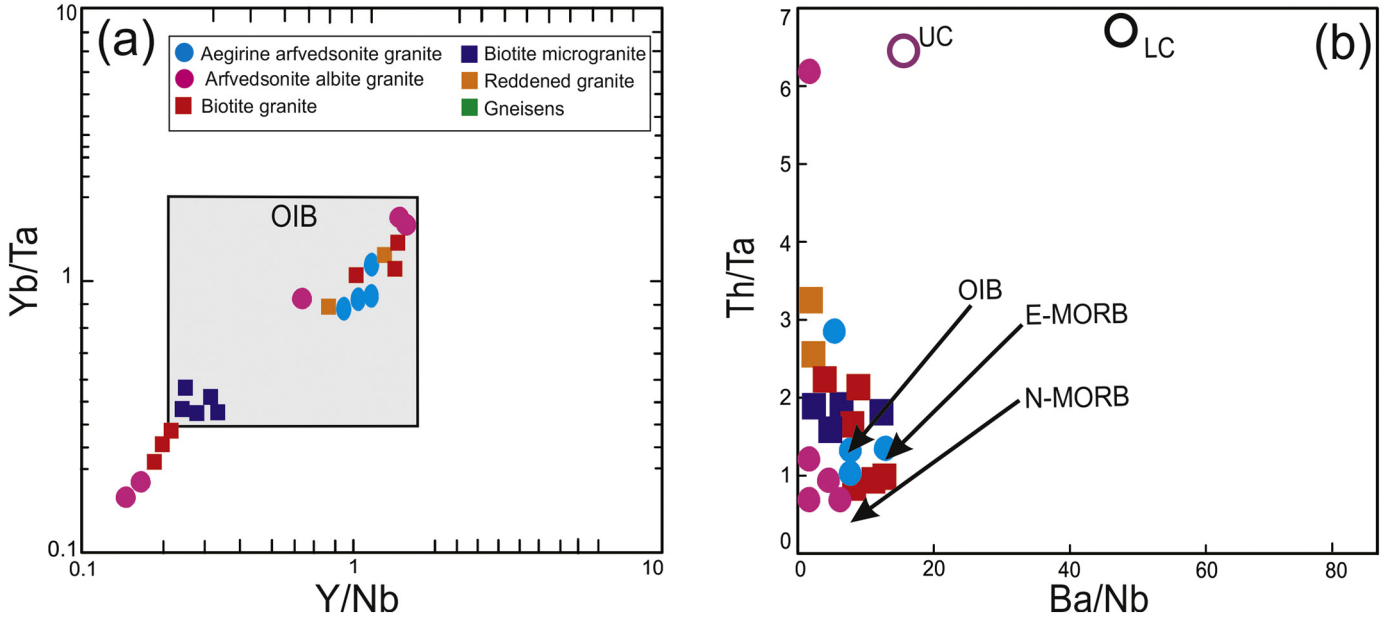

Fig. 12. Other discriminant diagrams for the Ririwai A-type granites. Fig. 12 (a) Y/Nb vs. Yb/Ta, and Fig. 12 (b) Ba/Nb vs. Th/Ta; (a) after Eby (1992). UC (upper crust) and LC (lower crust) fields were adapted from Rudnick and Gao (2013); N-MORB (normal mid-ocean ridge basalt), E-MORB (enriched mid-ocean ridge basalt), and OIB (ocean-island basalt) data are from Sun and McDonough (1989).

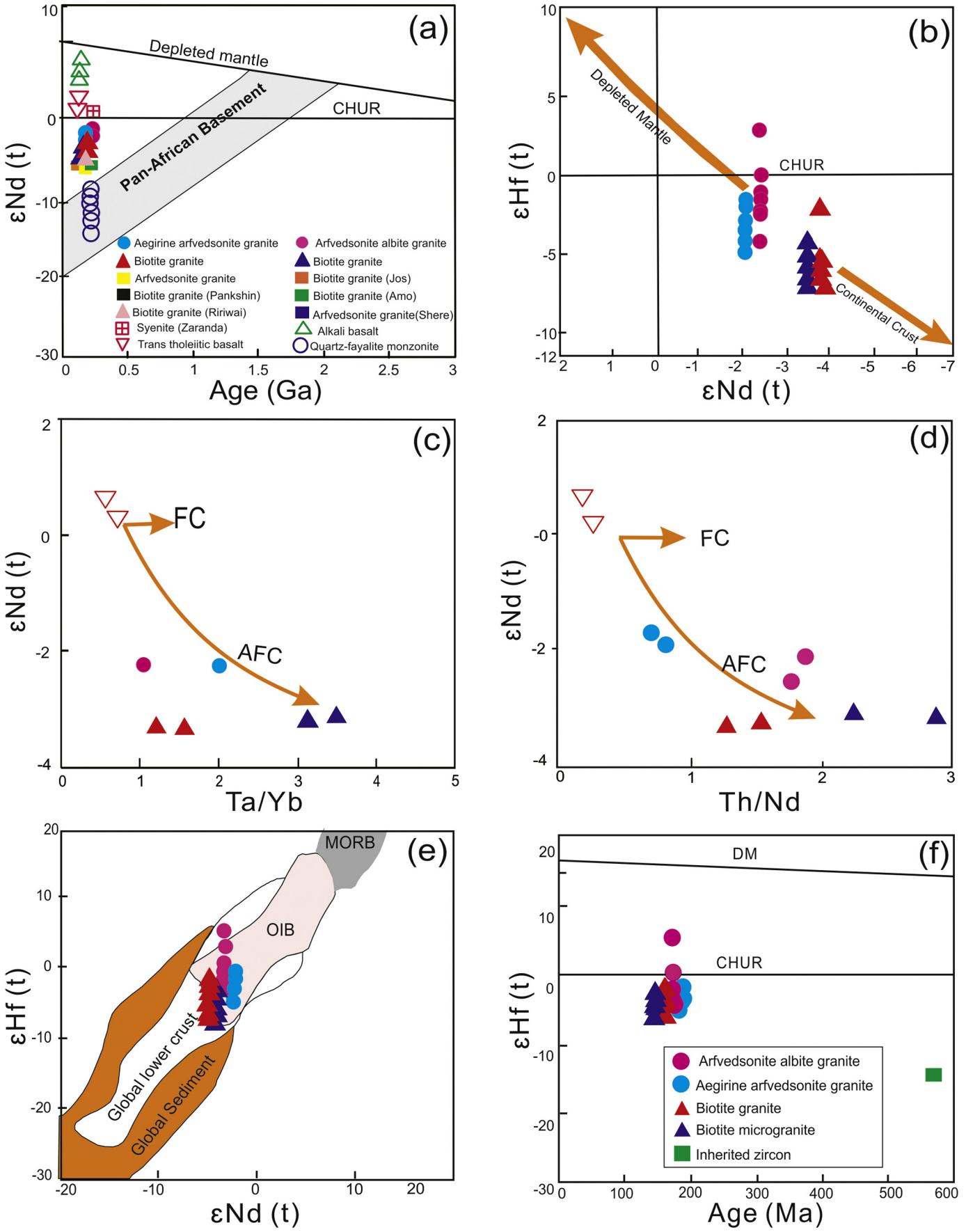

Fig. 13. Binary plots of (a) εNd(t) vs. age from this study and published data (Dickin et al., 1991) of five (5) Mesozoic anorogenic granite complexes in north-central Nigeria. Also plotted are published data of Mesozoic alkali and transitional basalt from Upper Benue trough, Northeastern Nigeria (Coulon et al., 1996), and Pan-African fayalite-bearing quartz monzonite (bauchite) recalculated from Dada et al. (1995). (b) εNd(t)vs. Ta/Yb, (c) εNd(t) vs Th/Nd (e) εHf(t) vs. εNd(t), (f) εHf(t) vs. age, and (d) $^{176}Hf/^{177}Hf$ vs. age discrimination plots. Estimated values of εHf(t) and εNd(t) for global lower crust and sediment were taken from Wang et al. (2016).

("bauchite"), considered by Brown and Bowden (1973) as the likely parental source for Nigerian A-type granites, yields significantly lower εNd (t) at 172 Ma (−8.4 to −13) and, therefore, is unlikely to have been the major component of the Ririwai A-type magmas (Supplementary Table 1). The low Y/Nb (<1.2) and Th/Ta ratios (~2) (Fig. 12a, b) in the Ririwai granites, except for the arfvedsonite albite granite, suggest that they were probably derived from OIB-like mantle sources (cf. Eby, 1992).

Neodymium isotope data are not available for the olivine basalt (R2) of the Ririwai complex, but Mesozoic (147–109 Ma) basalts of the Benue Trough can serve as proxies for the subcontinental lithospheric mantle in eastern Nigeria. Two discrete evolutionary trends were identified: (1) an alkaline series characterized by high, yet variable, εNd (t) values (+7.2 to +2.9), derived from mixed N-MORB, HIMU, and EM2 sources, (2) a transitional tholeiitic series characterized by lower εNd(t) (+0.7 to +1.4), derived largely from an EM1 source with a minor EM2 contribution (Coulon et al., 1996). In order to assess possible contributions of the mantle sources of these Mesozoic basalts to the genesis of Ririwai A-type granites, we re-evaluated previously published Sm—Nd isotope data for Nigerian anorogenic granites (Dickin et al., 1991) in conjunction with our data. In the εNd(t) vs. age plot (Fig. 13a), samples of syenite of the Zaranda complex plot above the CHUR and close to the transitional tholeiitic basalts, suggesting an enriched OIB mantle source without crustal contamination. All Nigerian A-type granites plot below CHUR, suggesting that they were derived from enriched mantle with contributions from the Pan-African basement through combined crustal assimilation and fractional crystallization (e.g., Kerr and Fryer, 1993; Trumbull et al., 2004; Siegel et al., 2017; Fig. 13c-d).

The Ririwai A-type granites display a wide range of zircon εHf(t). Zircons from the peralkaline granites yield εHf(t) ranging from −5.80 to −1.36, and zircons from the aluminous granites yield εHf(t) ranging from −7.83 to −2.35 (Table 3). With the exception of hydrothermally altered zircons, all Ririwai εHf(t) plot below the CHUR but above the field of granites derived from partial melting of ancient crustal materials (Fig. 13e-f) (e.g., Kemp et al., 2007). Hydrothermally altered zircons of the arfvedsonite albite granite yield more radiogenic εHf(t) values (+0.02 to +5.31) that are unlikely to represent source signatures.

6.3.2. Magmatic evolutionary processes

Compositional variation within granitic suites is a function of magma source composition as well as of petrogenetic processes such as fractional crystallization, wall-rock assimilation, fluid-rock interactions, and magma mixing (Li et al., 2018a). The evolutionary trend of a magma is largely controlled by the stability of crystallizing phases, which in turn depends on prevailing physicochemical conditions such as temperature, pressure, and water (P_{H2O}) and oxygen fugacities (Bachmann and Bergantz, 2008). Given the absence of large-scale rifting during emplacement of the Ririwai A-type suite, magma evolution probably followed a polybaric path that may have commenced with magma ponding beneath the lower crust, where significant fractionation of high-pressure phases such as olivine and pyroxene may have occurred (e.g., Bonin, 2007). This scenario can account for the exceedingly low contents of MgO and CaO in the Ririwai A-type suite. However, as is typical of most sub-volcanic ring complexes, the bulk of magma evolution may have occurred at fairly low pressures near the middle-upper crustal boundary (Siegel et al., 2018). Under these conditions, including the low P_{H2O} typical of within-plate A-type magmas, feldspars would the dominant fractionating minerals and, to a lesser degree, apatite would also be fractionated, as evidenced by strong depletions of Eu, Sr, Ba, and P_2O_5 (Table 1). This magmatic evolutionary trend, marked by strong feldspar crystallization coupled with limited crustal assimilation, could have given rise to the Ririwai peralkaline granites. As in most mineralized A-type granites, fluorine probably played a significant role in transporting REE and HFSE as fluoride complexes in the Ririwai A-type magmas (e.g., Dostal et al., 2014; Linnen et al., 2014). However, late-stage crystallization of cryolite and fluorite probably led to breakdown of REE and HFSE fluoride complexes near the solidus of the highly evolved peralkaline arfvedsonite albite granites. Consequently, these granites exhibit a convex (M-type) La—Nd tetrad effect and show increasing whole-rock concentrations of HFSE as well as high HREE/LREE ratios (e.g., Veksler et al., 2005; Fig. 6a, c). The mineral cryolite is unique in developing a concave (i.e., W-type) tetrad effect and, upon crystallization, it leaves a complimentary M-type tetrad effect in the residual magma (Veksler et al., 2005).

Formation of the alkali-calcic aluminous granites from the same parental melt that crystallized the peralkaline granites requires either metasomatism at subsolidus stage or contamination by a crustal component (Frost and Frost, 2011). According to Martin and Bowden (1981), the Ririwai metaluminous biotite granitic melt evolved from a mildly peralkaline magma through significant alkali loss. Subsequent metasomatism by K-rich fluids led to replacement of early micas by greenish micas (Fig. 3i-j) and to peraluminous reddened granite. A similar scenario has been inferred for the peraluminous granites in southeastern Kwandonkaya ring complex (Sakoma and Martin, 2011). However, the possibility of crustal contamination should not be discounted. For instance, alkali-calcic to calcic biotite microgranites, though relatively unaffected by K-metasomatism, are also notably peraluminous, consistent with crustal assimilation rather than metasomatic transformation (Frost and Frost, 2011). Compared to the peralkaline granites (εNd(t) = −2.28 to −1.20; εHf(t) = −5.80 to −1.36), the lower εNd(t) (−3.55 to −3.26) and εHf(t) (−7.83 to −2.35) values of the Ririwai aluminous granites suggest significant crustal assimilation/contamination during their formation.

6.4. Implications for mineralization

A notable feature of the Nigerian Younger Granite Province is the association with Sn-Nb-Zn mineralization. It is widely accepted that the formation of economic concentrations of these metals (in particular, Sn and Nb) requires a combination of favorable factors, including magma source composition, extensive fractional crystallization, and the presence of a halogen (e.g., F) as well as other volatiles (Dostal et al., 2014; Li et al., 2018a, 2018b; Romer and Kröner, 2016). The OIB-type mantle source is known to be highly enriched in HFSE and REE (Dostal et al., 2014; Eby, 1992) and may have contributed the bulk of Nb and, possibly, F to the Ririwai A-type granite magmas. In addition, with moderate crustal assimilation due to slow magma ascent through thick crust or protracted evolutionary history in a shallow magma chamber, the source magmas may have become enriched in Sn and Zn (e.g., Li et al., 2018a). The presence in biotite granite of inherited zircon crystals with an Ediacaran age of 590 ± 5 Ma, similar to the ~550 Ma Sn-Nb-Ta mineralized pegmatites in the nearby Wamba area (Küster, 1990), suggests that assimilation of (pegmatitic?) Pan-African basement contributed to the Sn–Nb–Zn mineralization of the aluminous Ririwai granites.

The high F content of the Ririwai A-type magmas, as indicated by the present of accessory fluorite, probably enhanced the solubility of Sn and Nb, because F can effectively form stable complexes with these metals facilitating their transport in a granitic melt (Linnen et al., 2014; Migdisov et al., 2016). Although the parent magmas of the Ririwai A-type granite were probably generated under water-deficient conditions (typical of within-plate A-type granites, e.g., Bonin, 2007), it is likely that the magmas became fluid-saturated following emplacement at an epizonal level and extensive fractional crystallization, as indicated by late-stage crystallization of arfvedsonite in the peralkaline granites (e.g., Dostal et al., 2014). Consequently, resurgent boiling as a result of volatile saturation may have led to exsolution of a fluorine-bearing fluid (e.g., Sakoma and Martin, 2011), a process that was accompanied by extensive fluid-rock interactions. In the peralkaline arfvedsonite albite granite, high F concentrations favored crystallization of cryolite as well as pyrochlore (Ogunleye et al., 2006). However, considering that alkali amphibole (arfvedsonite) crystallized at the late magmatic

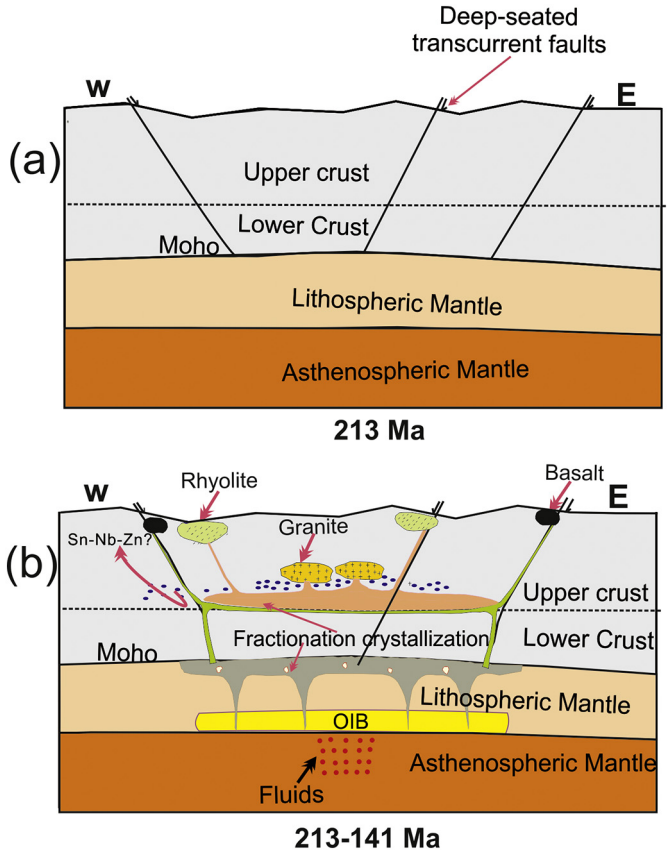

Fig. 14. A tectonic-magmatic-metallogenic model illustrating the emplacement of Jurassic A-type granites suites in Nigeria (modified from Lameyre, 1988). (a) 213 Ma; (b) between 213 Ma and 141 Ma. See text for detailed explanations.

stage, it may have taken up most of the Sn in the melt, as indicated by increasing whole-rock concentrations of Sn in the arfvedsonite albite granite (Table 1). In contrast, in the aluminous granites, multi-stage fluid-rock interaction was accompanied by deposition of economic concentrations of tin, columbite, and zinc.

6.5. A tectonomagmatic metallogenesis model

Ririwai A-type granites are within-plate granitoids corresponding to A1 granites, implying no direct relationship to a major orogeny (Black et al., 1985; Black and Liégeois, 1993). Previous Rb—Sr studies have shown that the Niger-Nigeria anorogenic ring complexes exhibit a N-S decreasing age trend from ~480–400 Ma in the Aïr Massif, Niger Republic, to 213–141 Ma in northern Nigeria (Bowden et al., 1976; Rahaman et al., 1984). Zircon U—Pb age dating (this study) has revealed that the Ririwai A-type granites were emplaced from 176 ± 2.3 to 169.6 ± 0.75 Ma, which, within error limits, closely matches the earlier Rb—Sr emplacement ages (Van Breemen et al., 1975).

Based on space-time migration of Nigerian anorogenic centres, Rahaman et al. (1984) demonstrated their arrayal along ENE-WSW and NNW-SSE transcurrent faults linked to N-S-trending mega-shear zones (Black and Liégeois, 1993). A direct correlation between periods of anorogenic igneous activity and rapid changes in African Plate motions has been noted in earlier studies (Bailey and Woolley, 2005; Black et al., 1985). Any abrupt change in plate motion direction can reactivate lithospheric shear zones and open associated oblique sets of transcurrent faults (Fig. 14a). Lithospheric fracturing can release pressure and channel hot metasomatic fluids upward, resulting in partial melting and magma generation at the base of the lithosphere (Black et al., 1985). Periodic opening and closure of lithospheric faults can account for apparent age migration in the Nigerian anorogenic complexes (e.g., Lameyre, 1988). Emplacement of the Nigerian ring complexes can, therefore, be linked to the transtensional regime generated prior to late Jurassic breakup of Gondwana, leading to reactivation of shear zones and opening of associated transcurrent faults, a mechanism similar to that responsible for pull-apart basins (Benkhelil, 1989). Thus, the compositional heterogeneity and Sn-Nb-Zn mineralization of the Ririwai granite complex imply extensive crystal fractionation coupled with crustal assimilation and late-stage hydrothermal fluids activity (Fig. 14b).

7. Conclusions

1. Peralkaline and aluminous A-type granites of the Ririwai Complex were emplaced between 176 ± 2.3 Ma and 169.6 ± 0.75 Ma, corresponding to Toarcian-Bajocian (Early to Middle Jurassic) ages.
2. Whole-rock Sm—Nd (−3.55 to −1.2) and zircon Hf isotopic (−7.8 to −1.36) data indicate that both peralkaline and aluminous granites formed from extensively differentiated magmas derived from enriched (OIB-like) mantle sources that were slightly modified through assimilation of the Pan-African upper crust into which the granites were emplaced.
3. The Ririwai A-type granites are anorogenic, and their parental melt was generated within a transtensional regime prior to the Late Jurassic breakup of Gondwana, leading to reactivation of major lithospheric shear zones and opening of associated transcurrent faults. This, in turn, triggered pressure release, partial melting, and melt generation at the base of the lithosphere.
4. Sn-Nb-Zn mineralization in the Ririwai granite complex resulted from complex magmatic evolutionary processes involving extensive fractional crystallization coupled with crustal assimilation and late-stage hydrothermal alteration.

Acknowledgments

We thank Sa'ad Ahmed of the Department of Geology, Ahmadu Bello University, Zaria, Nigeria, who assisted with sample collection at Ririwai. The research was funded by the National Science Foundation of China (Grant No. 41502067). The manuscript benefitted immensely from editorial handling by editor-in-chief Michael Roden and constructive reviews by Robert Trumbull and an anonymous reviewer.

Appendix A. Supplementary data

Supplementary data to this article can be found online at https://doi.org/10.1016/j.lithos.2019.05.003.

References

Ahmed, H.A., Ma, C., Wang, L., Garba, I., Girei, M.B., Vincent, V.I., 2019. Geochronology, petrogenesis and tectonic implication of A-type granite from Zaranda (North-Central Nigeria). In: Doronzo, et al. (Eds.), Petrogenesis and Exploration of the Earth's Interior, Advances in Science, pp. 17–20 (Technology & Innovation, Proceedings of the 1st Springer Conference of the Arabian Journal of Geosciences).

Bachmann, O., Bergantz, G.W., 2008. Rhyolites and their source mushes across tectonic settings. J. Petrol. 49, 2277–2285.

Bailey, D.K., Woolley, A.R., 2005. Repeated, synchronous magmatism within Africa: timing, magnetic reversals, and global tectonics. Geol. Soc. Am. Spec. Pap. 388, 365–377. https://doi.org/10.1130/2005.2388(22).

Belousova, E.A., Griffin, W.L., O'Reilly, S.Y., Fisher, N.I., 2002. Igneous zircon: trace element composition as an indicator of source rock type. Contrib. Mineral. Petrol. 143, 602–622. https://doi.org/10.1007/s00410-002-0364-7.

Belousova, E.A., Griffin, W.L., O'Reilly, S.Y., 2006. Zircon crystal morphology, trace element signatures and Hf isotope composition as a tool for petrogenetic modelling: examples from Eastern Australian granitoids. J. Petrol. 47, 329–353. https://doi.org/10.1093/petrology/egi077.

Benkhelil, J., 1989. The origin and evolution of the cretaceous Benue Trough (Nigeria). J. Earth Sci. 8, 251–282. https://doi.org/10.1016/S0899-5362(89)80028-4.

Black, R., Liégeois, J.P., 1993. Cratons, mobile belts, alkaline rocks and continental lithospheric mantle: the Pan-African testimony. J. Geol. Soc. Lond. 150, 89–98.

Black, R., Lameyre, J., Bonin, B., 1985. The structural setting of alkaline complexes. J. Afr. Earth Sci. 3, 5–16. https://doi.org/10.1016/0899-5362(85)90019-3.

Bonin, B., 2007. A-type granites and related rocks: evolution of a concept, problems and prospects. Lithos 97, 1–29. https://doi.org/10.1016/j.lithos.2006.12.007.

Bonin, B., 2012. Extra-terrestrial igneous granites and related rocks: a review of theiroccurrence and petrogenesis. Lithos 153, 2–24. https://doi.org/10.1016/j.lithos.2012.04.007.

Bowden, P., 1985. The geochemistry and mineralization of alkaline ring complexes in Africa (a review). J. Afr. Earth Sci. 3, 17–39. https://doi.org/10.1016/0899-5362(85)90020-X.

Bowden, P., Kinnaird, J.A., 1984. The petrology and geochemistry of alkaline granites from Nigeria. Phys. Earth Planet. Inter. 35, 199–211. https://doi.org/10.1016/0031-9201(84)90043-8.

Bowden, P., Van Breemen, O., Hutchinson, J., Turner, D.C., 1976. Paleozoic and Mesozoic age trends for some ring complexes in Niger and Nigeria. Nature 259, 297–299.

Bowden, P., Black, R., Martin, R.F., Ike, E.C., Kinnaird, J.A., Batchelor, R.A., 1987. Niger-Nigerian alkaline ring complexes: a classic example of African Phanerozoic anorogenic mid-plate magmatism. Geol. Soc. Lond. Spec. Publ. 30, 357–379. https://doi.org/10.1144/GSL.SP.1987.030.01.17.

Brown, G.C., Bowden, P., 1973. Experimental studies concerning the genesis of the Nigerian Younger granites. Contrib. Mineral. Petrol. 40, 131–139. https://doi.org/10.1007/BF00378170.

Coulon, C., Vidal, P., Dupuy, C., Baudin, P., Popoff, M., Maluski, H., Hermitte, D., 1996. The Mesozoic to early Cenozoic magmatism of the Benue Trough (Nigeria); geochemical evidence for the involvement of the St Helena Plume. J. Petrol. 37, 1341–1358. https://doi.org/10.1093/petrology/37.6.1341.

Creaser, R.A., Price, R.C., Wormald, R.J., 1991. A-type granites revisited: assessment of a residual-source model. Geology 9, 163–166. https://doi.org/10.1130/0091-7613(1991)019<0163:ATGRAO>2.3.CO;2.

Dada, S.S., Briqueu, L., Harms, U., Lancelot, J.R., Matheis, G., 1995. Charnockitic and monzonitic Pan-African series from north-Central Nigeria: trace-element and Nd, Sr, Pb isotope constraints on their petrogenesis. Chem. Geol. 124, 233–252. https://doi.org/10.1016/0009-2541(95)00010-J.

Dall'Agnol, R., Frost, C.D., Rämö, O.T., 2012. IGCP Project 510 "A-type Granites and Related Rocks through Time": project vita, results, and contribution to granite research. Lithos 93, 215–233. https://doi.org/10.1016/j.lithos.2012.08.003.

De La Roche, H., Leterrier, J., Grande-Claude, P., Marchal, M., 1980. A classification of volcanic and plutonic rocks using R1-R2 diagrams and major element analyses: its relationship with current nomenclature. Chem. Geol. 19, 183–210.

Dickin, A.P., Halliday, A.N., Bowden, P., 1991. A Pb, Sr and Nd isotope study of the basement and mesozoic ring complexes of the Jos Plateau, Nigeria. Chem. Geol. 94, 23–32. https://doi.org/10.1016/S0009-2541(10)80014-2.

Dostal, J., Kontak, D.J., Karl, S.M., 2014. The early Jurassic Bokan Mountain peralkaline granitic complex (southeastern Alaska): geochemistry, petrogenesis and rare-metal mineralization. Lithos 202–203, 395–412.

Eby, G.N., 1992. Chemical subdivision of the A-type granitoids: petrogenetic and tectonic implications. Geology 20, 641–644. https://doi.org/10.1130/0091-7613(1992)020<0641:CSOTAT>2.3.CO;2.

Ferré, E.C., Caby, R., 2007. Granulite facies metamorphism and charnockite plutonism: examples from the Neoproterozoic Belt of northern Nigeria. Proc. Geol. Assoc. 118, 47–54. https://doi.org/10.1016/S0016-7878(07)80046-0.

Ferré, E.C., Caby, R., Peucat, J.J., Capdevila, R., Monié, P., 1998. Pan-African, post-collisional, ferro-potassic granite and quartz-monzonite plutons of Eastern Nigeria. Lithos 45, 255–279. https://doi.org/10.1016/S0024-4937(98)00035-8.

Frost, C.D., Frost, B.R., 2011. On ferroan (A-type) granitoids: their compositional variability and modes of origin. J. Petrol. 52, 39–53. https://doi.org/10.1093/petrology/egq070.

Frost, B.R., Barnes, C.G., Collins, W.J., Arculus, R.J., Ellis, D.J., Frost, C.D., 2001. A geochemical classification for granitic rocks. J. Petrol. 42, 2033–2048.

Griffin, W.L., Wang, X., Jackson, S.E., Pearson, N.J., O'Reilly, S.Y., Xu, X., Zhou, X., 2002. Zircon chemistry and magma mixing, SE China: in-situ analysis of Hf isotopes, Tonglu and Pingtan igneous complexes. Lithos 61, 237–269. https://doi.org/10.1016/S0024-4937(02)00082-8.

Gysi, A.P., Williams-Jones, A.E., Collins, P., 2016. Lithogeochemical vectors for hydrothermal processes in the Strange Lake peralkaline granitic REE-Zr-Nb deposit. Econ. Geol. 111, 1241–1276.

Jacobson, R.R.E., McLeod, W.N., 1977. Geology of the Liruei, Banke and adjacent Younger Granite ring-complexes. Geol. Surv. Nigeria Bull. 33, 117.

Jacobson, R.R.E., McLeod, W.N., Black, R., 1958. Ring-complexes in the Younger Granite Province of northern Nigeria. Geol. Soc. Lond. Mem. 1, 5–71. https://doi.org/10.1144/GSL.MEM.1958.001.01.01.

Jahn, B., Wu, F., Capdevila, R., Martineau, F., Zhao, Z., Wang, Y., 2001. Highly evolved juvenile granites with tetrad REE pattern: the Woduhe and Baerzhe granites from the Great Xing'an Mountains in NE China. Lithos 59, 171–198.

Kaur, P., Chaudhri, N., Hofmann, A.W., Raczek, I., Okrusch, M., Skora, S., Baumgartner, L.P., 2012. Two-stage, extreme albitization of A-type granites from Rajasthan, NW India. J. Petrol. 53, 919–948.

Kemp, A.I.S., Wormald, R.J., Whitehouse, M.J., Price, R.C., 2005. HF isotopes in zircon reveal contrasting sources and crystallization histories for alkaline to peralkaline granites of Temora, southeastern Australia. Geology 33, 797–800. https://doi.org/10.1130/G21706.1.

Kemp, A.I.S., Hawkesworth, C.J., Foster, G.L., Paterson, B.A., Woodhead, J.D., Hergt, J.M., Gray, C.M., Whitehouse, M.J., 2007. Magmatic and crustal differentiation history of granitic rocks from Hf-O isotopes in zircon. Science 315, 980–983. https://doi.org/10.1126/science.1136154.

Kerr, A., Fryer, B.J., 1993. Nd isotope evidence for crust-mantle interaction in the generation of A-type granitoid suites in Labrador, Canada. Chem. Geol. 104, 39–60. https://doi.org/10.1016/0009-2541(93)90141-5.

Kinnaird, J.A., Bowden, P., 1991. Magmatism and mineralization associated with Phanerozoic anorogenic plutonic complexes of the African plate. In: Kampunzu, A.B., Lubala, R.T. (Eds.), Magmatism in Extensional Structural Settings. Springer-Verlag, Berlin, p. 637.

Kinnaird, J.A., Bowden, P., Ixer, R.A., Odling, N.W.A., 1985. Mineralogy, geochemistry and mineralization of the Ririwai complex, northern Nigeria. J. Afr. Earth Sci. 3, 185–222. https://doi.org/10.1016/0899-5362(85)90036-3.

Kinnaird, J.A., Nex, P.A.M., Milani, L., 2016. Tin in Africa. Episodes 39, 362–380. https://doi.org/10.18814/epiiugs/2016/v39i2/95783.

Küster, D., 1990. Rare-metal pegmatites of Wamba, Central Nigeria – their formation in relationship to late Pan-African granites. Mineral. Deposita 25, 25–33. https://doi.org/10.1007/BF03326380.

Lameyre, J., 1988. Granite settings and tectonics. Rend. Soc. Ital. Mineral. Petrol. 43, 215–236.

Le Maitre, R.W., 1989. A Classification of Igneous Rocks and Glossary of Terms: Recommendations of the IUGS Subcommission on the Systematics of Igneous Rocks. Blackwell, Oxford, pp. 130–171.

Li, X.H., McCulloch, M.T., 1998. Geochemical characteristics of cretaceous mafic dikes from northern Guangdong, SE China: age, origin and tectonic significance. In: Flower, M.F.J., Chung, S.-L., Lo, C.-H., Li, Z.X., Li, X.H., Lee, T.-Y. (Eds.), Mantle Dynamics and Plate Interaction in East Asia Volume 27: Geodynamics Series. Am. Geophys. Union, Washington D.C, pp. 405–419.

Li, H., Palinkaš, L.A., Watanabe, K., Xi, X.S., 2018a. Petrogenesis of Jurassic A-type granites associated with Cu-Mo and W-Sn deposits in the central Nanling region, South China: relation to mantle upwelling and intra-continental extension. Ore Geol. Rev. 92, 449–462. https://doi.org/10.1016/j.oregeorev.2017.11.029.

Li, H., Wu, J.H., Evans, N.J., Jiang, W.C., Zhou, Z.K., 2018b. Zircon geochronology and geochemistry of the Xianghualing A-type granitic rocks: insights into multi-stage Sn-polymetallic mineralization in South China. Lithos 312–313, 1–20.

Linnen, R.L., Samson, I.M., Williams-Jones, A.E., Chakhmouradian, A.R., 2014. Geochemistry of the Rare Earth Element, Nb, Ta, Hf and Zr Deposits, in Treatise on Geochemistry, 13. 2nd edition. vol. 13 pp. 543–568.

Liu, Y.S., Hu, Z.C., Zong, K.Q., Gao, C.G., Gao, S., Xu, J., Chen, H.H., 2010. Reappraisement and refinement of zircon U-Pb isotope and trace element analyses by LA-ICP-MS. Chin. Sci. Bull. 55, 1535–1546.

Loiselle, M.C., Wones, D.R., 1979. Characteristics and origin of anorogenic granites. Geol. Soc. Am. Abstr. Programs 11, 468.

Ludwig, K.R., 2003. User's Manual for Isoplot 3.00: A Geochronological Toolkit for Microsoft Excel. p. 39.

Machado, N., Simonetti, A., 2001. U–Pb dating and Hf isotopic composition of zircon by laser ablation MC-ICP-MS. In: Sylvester, P. (Ed.), Principles and Applications of Laser-Ablation ICP-Mass Spectrometry in the Earth Sciences. Mineral. Assoc. Canada Short Course vol. 29, pp. 121–146.

Magaji, S.S., Martin, R.F., Ike, E.C., Ikpokonte, A.E., 2011. The Geshere syenite-peralkaline granite pluton: a key to understanding the anorogenic Nigerian Younger Granites and analogues elsewhere. Period. Mineral. 80, 199. https://doi.org/10.2451/2011PM0016.

Martin, R.F., 2006. A-type granites of crustal origin ultimately result from open-system fenitization-type reactions in an extensional environment. Lithos 91, 125–136. https://doi.org/10.1016/j.lithos.2006.03.012.

Martin, R.F., Bowden, P., 1981. Peraluminous granites produced by rock-fluid interaction in the Ririwai nonorogenic ring-complex, Nigeria: mineralogical evidence. Can. Mineral. 19, 65–82.

Martin, R.F., Sokolov, M., Magaji, S.S., 2012. Punctuated anorogenic magmatism. Lithos 152, 132–140. https://doi.org/10.1016/j.lithos.2012.05.020.

Migdisov, A., Williams-Jones, A.E., Brugger, J., Caporuscio, F.A., 2016. Hydrothermal transport, deposition, and fractionation of the REE: experimental data and thermodynamic calculations. Chem. Geol. 439, 13–42.

Ngako, V., Njonfang, E., Aka, F.T., Affaton, P., Nnange, J.M., 2006. The North-South Paleozoic to Quaternary trend of alkaline magmatism from Niger-Nigeria to Cameroon: complex interaction between hotspots and Precambrian faults. J. Afr. Earth Sci. 45, 241–256. https://doi.org/10.1016/j.jafrearsci.2006.03.003.

Ogunleye, P.O., Garba, I., Ike, E.C., 2006. Factors contributing to enrichment and crystallization of niobium in pyrochlore in the Kaffo albite arfvedsonite granite, Ririwai complex, Younger Granites province of Nigeria. J. Afr. Earth Sci. 44, 372–382. https://doi.org/10.1016/j.jafrearsci.2005.12.006.

Pearce, J.A., Harris, N.W., Tindle, A.G., 1984. Trace element discrimination diagrams for the tectonic interpretation of granitic rocks. J. Petrol. 25, 956–983. https://doi.org/10.1093/petrology/25.4.956.

Peccerillo, A., Taylor, S.R., 1976. Geochemistry of Eocene calc-alkaline volcanic rocks from the Kastamonu area, northern Turkey. Contrib. Mineral. Petrol. 58, 63–81.

Rahaman, M.A., Van Breemen, O., Bowden, P., Bennett, J.N., 1984. Age migration of anorogenic ring-complexes in northern Nigeria. J. Geol. 92, 173–184.

Romer, R.L., Kröner, U., 2016. Phanerozoic tin and tungsten mineralization - tectonic controls on the distribution of enriched protoliths and heat sources for crustal melting. Gondwana Res. 31, 60–95. https://doi.org/10.1016/j.gr.2015.11.002.

Rudnick, R.L., Gao, S., 2013. Composition of the continental crust. Treatise on Geochemistry, 2nd edition 3, pp. 1–64. https://doi.org/10.1016/B978-0-08-095975-7.00301-6.

Sakoma, E.M., Martin, R.F., 2011. Frozen disequilibrium in the feldspar mineralogy of the Kwandonkaya anorogenic complex, Nigerian A-type Granite Province. Can. Mineral. 49, 967–982. https://doi.org/10.3749/canmin.49.4.967.

Shand, S.J., 1943. Eruptive Rocks: Their Genesis, Composition, Classification, and Their Relation to Ore-Deposits, With a Chapter on Meteorites. John Wiley & Sons, New York, p. 350.
Siegel, K., Williams-Jones, A.E., Stevenson, R., 2017. A Nd- and O-isotope study of the REE-rich peralkaline Strange Lake granite: implications for Mesoproterozoic A-type magmatism in the Core Zone (NE-Canada). Contrib. Mineral. Petrol. 172, 54–77. https://doi.org/10.1007/s00410-017-1373-x.
Siegel, K., Vasyukova, O.V., Williams-Jones, A.E., 2018. Magmatic evolution and controls on rare metal-enrichment of the Strange Lake A-type peralkaline granitic pluton, Québec-Labrador. Lithos 308–309, 34–52.
Spitz, G., Darling, R., 1978. Major and minor elements lithochemical anomalies surrounding the Louvern copper deposits, Vald'Or, Quebec. Can. J. Earth Sci. 15, 1161–1169.
Sun, S., McDonough, W.F., 1989. Chemical and isotopic systematics of oceanic basalts: implications for mantle compositions and processes. In: Saunders, A.D., Norry, M.J. (Eds.), Magmatism in the Ocean Basalts. vol. 42. Geol. Soc. Lond. Spec. Publ, pp. 313–345.
Sylvester, P.J., 1989. Post-collisional alkaline granites. J. Geol. 97, 261–280. https://doi.org/10.1086/629302.
Taylor, S.R., McLennan, S.M., 1985. The Continental Crust: Its Composition and Evolution. Oxford Press, Blackwell, pp. 1–31.
Trumbull, R.B., Harris, C., Frindt, S., Wigand, M., 2004. Oxygen and neodymium isotope evidence for source diversity in cretaceous anorogenic granites from Namibia and implications for A-type granite genesis. Lithos 73, 21–40. https://doi.org/10.1016/j.lithos.2003.10.006.
Van Breemen, O., Hutchinson, J., Bowden, P., 1975. Age and origin of the Nigerian Mesozoic granites: a Rb-Sr isotopic study. Contrib. Mineral. Petrol. 50, 157–172. https://doi.org/10.1007/BF00371037.
Veksler, I.V., Dorfman, A.M., Kamenetsky, M., Dulski, P., Dingwell, D.B., 2005. Partitioning of lanthanides and Y between immiscible silicate and fluoride melts, fluorite and cryolite and the origin of the lanthanide tetrad effect in igneous rocks. Geochim. Cosmo. Chim. Acta. 69, 2847–2860.
Wang, C., Lu, Y., He, X., Wang, Q., Zhang, J., 2016. The Paleoproterozoic diorite dykes in the southern margin of the North China Craton: insight into rift-related magmatism. Precambrian Res. 277, 26–46. https://doi.org/10.1016/j.precamres.2016.02.009.
Watson, E.B., Harrison, T.M., 1983. Zircon saturation revisited temperature and composition effects in a variety of crustal magma types. Earth Planet. Sci. Lett. 64, 295–305.
Whalen, J.B., Currie, K.L., Chappell, B.W., 1987. A-type granites: geochemical characteristics, discrimination and petrogenesis. Contrib. Mineral. Petrol. 95, 407–419. https://doi.org/10.1007/BF00402202.
Whalen, J.B., Jenner, G.A., Longstaffe, F.J., Robert, F., Gariépy, C., 1996. Geochemical and isotopic (O, Nd, Pb and Sr) constraints on A-type granite petrogenesis based on the Topsails igneous suite, Newfoundland Appalachians. J. Petrol. 37, 1463–1489. https://doi.org/10.1093/petrology/37.6.1463.